# East Atlantic (EA) and North Atlantic Oscillation (NAO) interplay over the Iberian Peninsula for the last two millennia

Sánchez-López G.[a*], Hernández A.[b], Pla-Rabes S.[c], Trigo R.M.[b],Toro M.[d], Granados I.[e], Sáez A.[f], Masqué P.[g,h,i], Pueyo J.J.[f], Rubio-Inglés M.J.[a], Giralt S.[a]

[a]Institute of Earth Sciences Jaume Almera (ICTJA - CSIC), Lluís Solé i Sabarís s/n, E-08028 Barcelona, Spain.

[b]Instituto Dom Luiz (IDL), Faculdade de Ciências, Universidade de Lisboa, Lisbon 1749-016, Portugal.

[c]Centre de Recerca Ecològica i Aplications Forestals (CREAF), E-08193, Cerdanyola del Vallés, Spain.

[d]Centro de Estudios Hidrográficos (CEDEX), Paseo Bajo Virgen del Puerto, 3, E- 28005 Madrid, Spain.

[e]Centro de Investigación, Seguimiento y Evaluación. Parque Nacional de la Sierra de Guadarrama. Cta. M-604, Km 27.6 E-28740 Rascafría, Madrid, Spain.

[f] Faculty of Geology, Universitat de Barcelona, Martí i Franquès s/n, E-08028 Barcelona, Spain.

[g]Departament de Física and Institut de Ciència i Tecnologia Ambientals, Universitat Autònoma de Barcelona, 08193 Bellaterra, Barcelona, Spain

[h] School of Science, Centre for Marine Ecosystems Research, Edith Cowan University, Joondalup WA 6027

[i]School of Physics and Oceans Institute, University of Western Australia, 35 Stirling Highway, Crawley 6009

*Corresponding author. Institute of Earth Sciences Jaume Almera (ICTJA-CSIC), Lluís Solé i Sabarís s/n, E-08028 Barcelona, Spain. Tel. +34 93 409 54 10. Fax: +34 93 411 00 12. E-mail address: guiomarus@gmail.com

**Abstract**

A multi-proxy characterization of the uppermost sedimentary infill of an Iberian alpine lake (Cimera, 2140 m a.s.l.) was performed to establish the climatic and environmental conditions for the Iberian Central Range (ICR) over the last two millennia. This multi-proxy characterization was used to reconstruct the intense runoff events, lake productivity and soil erosion in the lake catchment and interpret these factors in terms of temperature and precipitation variability. The Roman Period (RP; 200 BC – 500 AD) beginning was characterized by an alternation between cold and warm periods as indicated by short-lived oscillations of intense runoff conditions and soil erosion, although warm conditions dominated the end of the period and the Early Middle Age (EMA; 500 – 900 AD) onset in the ICR. A noticeable decrease in intense runoff events and a progressive decrease in soil erosion during the late EMA indicated a shift to colder temperatures. In terms of precipitation, both the RP and EMA climate periods displayed a transition from dry to wet conditions that led to a decrease in lake productivity. The Medieval Climate Anomaly (MCA; 900 – 1300 AD) was characterized by warm and dry conditions with frequent intense runoff episodes and increases in lake productivity and soil erosion, whereas the Little Ice Age (LIA; 1300 – 1850 AD) showed the opposite characteristics. The Industrial Era (1850 – 2012 AD) presented an increase in lake productivity that likely demonstrates the influence of global warming.

The spatiotemporal integration of the Cimera record with other Iberian reconstructions has been used to identify the main climate drivers over this region. During the RP and EMA, N–S and E–W humidity gradients were dominant, whereas during the MCA and LIA, these gradients were not evident. These differences could be ascribed to interactions between the North Atlantic Oscillation (NAO) and East Atlantic (EA) phases. During the RP, the general warm conditions and the W–E humidity gradient indicate a dominant interplay between a negative NAO phase and a positive EA phase ($NAO^-$–$EA^+$),

whereas the opposite conditions during the EMA indicate a $NAO^{+}$–$EA^{-}$ interaction. The dominant warm and arid conditions during the MCA and the cold and wet conditions during the LIA indicate the interplay of the $NAO^{+}$–$EA^{+}$ and $NAO^{-}$–$EA^{-}$, respectively. Furthermore, the higher solar irradiance and fewer tropical volcanic eruptions during the RP and MCA may support the predominance of the $EA^{+}$ phase, whereas the opposite scenario during the EMA and LIA may support the predominance of the $EA^{-}$ phase, which would favour the occurrence of frequent and persistent blocking events in the Atlantic region during these periods.

**Keywords:** alpine lake, Iberian climate, soil erosion, lacustrine sediments, NAO, EA

**Highlights**

We perform a high-resolution multiproxy study from Iberian alpine lake sediments

Climatic conditions for Iberian Central Range over the last two millennia

Climate gradients distinguished the Iberian Roman Period and the Early Middle Ages

Spatial homogeneous climate conditions depicted MCA and LIA in the Iberian region

The NAO and EA interactions drive climate patterns over Iberian Peninsula

## 1. INTRODUCTION

The climate of the Iberian Peninsula presents large interannual and interdecadal variability in addition to markedly strong seasonal cycles (Lionello, 2012). The intense interannual variability is responsible for the frequent occurrence of both wet and dry years and associated with the latitudinal displacement of storm tracks that is partially controlled by the jet stream positioning (Barry and Chorley, 2009). Over the last two decades, studies have shown with increasing accuracy that the location and magnitude of these weather systems is controlled by a small number of large-scale patterns or modes (e.g., Hurrell,

1995; Trigo et al., 2002; 2008). Among these modes, the North Atlantic Oscillation (NAO) is the most prominent and recurrent pattern of atmospheric variability over the middle and high latitudes of the Northern Hemisphere (Hurrell et al., 2003). The effects of the winter NAO on the Iberian Peninsula (IP) climate are more evident in the precipitation records than in the air temperature measurements (Castro-Díez et al., 2002; Trigo et al., 2002). In addition to the NAO, other North Atlantic-European modes of climate variability, such as the East Atlantic (EA) and Scandinavian (SCAND) patterns, are also known to play a significant role in modulating climate variables in the IP (Comas-Bru and McDermott, 2014; Jerez and Trigo, 2013; Trigo et al., 2008).

Lacustrine sedimentary records have been widely used to determine the environmental and climatic history of the IP. The most frequently studied lacustrine records are from low- and mid-lying altitude areas, such as the sedimentary records from Sanabria Lake (1000 m a.s.l.; Jambrina-Enríquez et al., 2014) and Enol Lake (1075 m a.s.l.; Moreno el at., 2010) in the northern IP; Arreo Lake (655 m a.s.l.; Corella et al., 2013), Estanya (670 m a.s.l.; Morellón et al. 2009, 2011; Riera et al., 2004) and Montcortès Lake (1027 m a.s.l.; Corella et al. 2011) in the Pre-Pyrenees; the Tablas de Daimiel wetland (616 m a.s.l.; Gil García et al., 2007) and Taravilla Lake (1100 m a.s.l.; Moreno et al., 2008) in the Central IP; and Zoñar Lake (300 m a.s.l.; Martín-Puertas et al. 2008, 2010; Valero-Garcés et al., 2006) in the southern IP. Reconstructions based on lacustrine sequences from low-altitude lakes usually face the additional challenge of distinguishing between climatic and anthropic signals (Barreiro-Lostres et al., 2015; Morellón et al., 2011; Valero-Garcés et al., 2006), whereas high-mountain lakes often present negligible anthropic influence because of the limited human activities in these remote areas; thus, their sedimentary records often contain more pristine climatic signals compared with the low-mountain records.

Therefore, climate reconstructions from the main Iberian mountain ranges have increased over the last decade, including reconstructions of the Pyrenees from Redon Lake

(2240 m a.s.l.; Pla and Catalan, 2005; Pla-Rabes and Catalan, 2011), Marboré Lake (2500 m a.s.l.; Salabarnada, 2011) and Basa de la Mora Lake (1914 m a.s.l.; Morellón et al., 2012; Moreno et al., 2012; Pérez-Sanz et al., 2013) and the southern Spain ranges (*Sierra Nevada)* from Laguna de Rio Seco (3020 m a.s.l.; Jiménez-Espejo et al., 2014). In addition, several environmental reconstructions of the Iberian Central Range (ICR) are based on palynological records from different peatlands (>1700 m a.s.l.; López-Sáez et al., 2014). However, to the best of our knowledge, only two climate reconstructions have been conducted from an alpine lake (Cimera Lake, 2140 m a.s.l.) located in the ICR, and they cover the last several centuries (Agustí-Panareda and Thompson, 2002; Granados and Toro, 2000).

Most of these climate reconstructions distinguish five main climatic periods for the last two millennia: the Roman Period (RP; 650 BC – 500 AD), the Early Middle Ages (EMA; 500 – 900 AD), the Medieval Climate Anomaly (MCA; 900 - 1300 AD), the Little Ice Age (LIA; 1300 - 1850 AD); and the so-called Industrial Era (1850 – 2012 AD). The studied records provide detailed information on the climatic evolution for specific time windows (e.g., MCA and LIA, Morellón et al., 2012; Moreno et al., 2012), whereas other periods (e.g., EMA and RP, Luterbacher et al., 2016) remain less studied. Furthermore, when comparing the environmental and climate information between the lowlands and highlands, it is clear that the spatial coverage of the latter must be improved.

The influence of the NAO on the lacustrine ecosystems of the IP has also been determined for these historical periods (e.g., Morellón et al., 2012; Moreno et al. 2012; Nieto-Moreno et al., 2011). These climate reconstructions commonly ascribe the warm and arid climate conditions of the MCA to the dominance of the positive phases of the NAO and the humid and cold conditions of the LIA to the dominance of the negative phases of this climate mode (Ortega et al., 2015; Trouet et al., 2009). Nevertheless, the role of the other climate modes in the climatic evolution as well as their interactions with the NAO over the

last millennia have not been well addressed. Within this scope, recent works based on limnological measurements from Iberian lakes (Hernández et al., 2015) and isotopic data for European precipitation (Comas-Bru et al., 2016) have gone a step further and assessed the sensitivity of these records to variations in these climate modes (e.g., NAO, EA and SCAND), although only for recent decades.

The objective of this study was to address the lack of climate data for the last two millennia in the ICR, a key region of the IP, by identifying and characterizing the main climate changes and their forcing mechanisms. For this purpose, we have applied a high-resolution multiproxy approach to sediments of an alpine lake (Cimera Lake). A comparison of the obtained paleoclimate record with other Iberian climate reconstructions was performed to determine the spatial and temporal climate variability over time and demonstrate that climactic reconstructions of the last two millennia of the IP should simultaneously consider the influence of the NAO as well as other climate forcings (e.g., the EA pattern).

## 2. STUDY SITE

### 2.1.- Regional setting

Cimera Lake is located in the southern branch of the ICR (Fig. 1a). This mountainous region is located left of the centre of the IP, extends approximately 700 km from NE to SW and presents elevations of up to ~2600 m a.s.l. The pre-Quaternary lithology of the region is primarily composed of late Palaeozoic igneous rocks (granite and gneiss), although slates are also present (De Vicente et al., 1994; Pedraza, 1994).

The climate of the ICR is an alpine type immersed in a Mediterranean climate with a strong continental influence (Durán et al., 2013). The arrival of Atlantic depressions from the SW frequently occur in fall, winter and spring; however, the Azores anticyclone is persistent and does not favour moisture transport from the west in summer. As a consequence, this regional climate is characterized by a significant amount of solid

precipitation and low temperatures in winter and warm and dry conditions in summer (Sánchez-López et al., 2015). The mean annual temperatures oscillate between 0 and 2 °C during the coldest month and between 20 – 22 °C during the hottest month. The total annual rainfall is ca. 1400 mm and occurs in the humid ombrotype region (Ninyerola et al., 2005; Palacios et al., 2012).

Figure 1. (a) Topographical map of the Iberian Peninsula showing the locations of different records involved in this study. (b) Topographic and (c) bathymetric maps of Cimera Lake according to Granados and Toro (2000); the red point indicates the location of the Cimera record used in this study (i.e., CIM12-04A). (d) UWITEC© gravity recovering system.

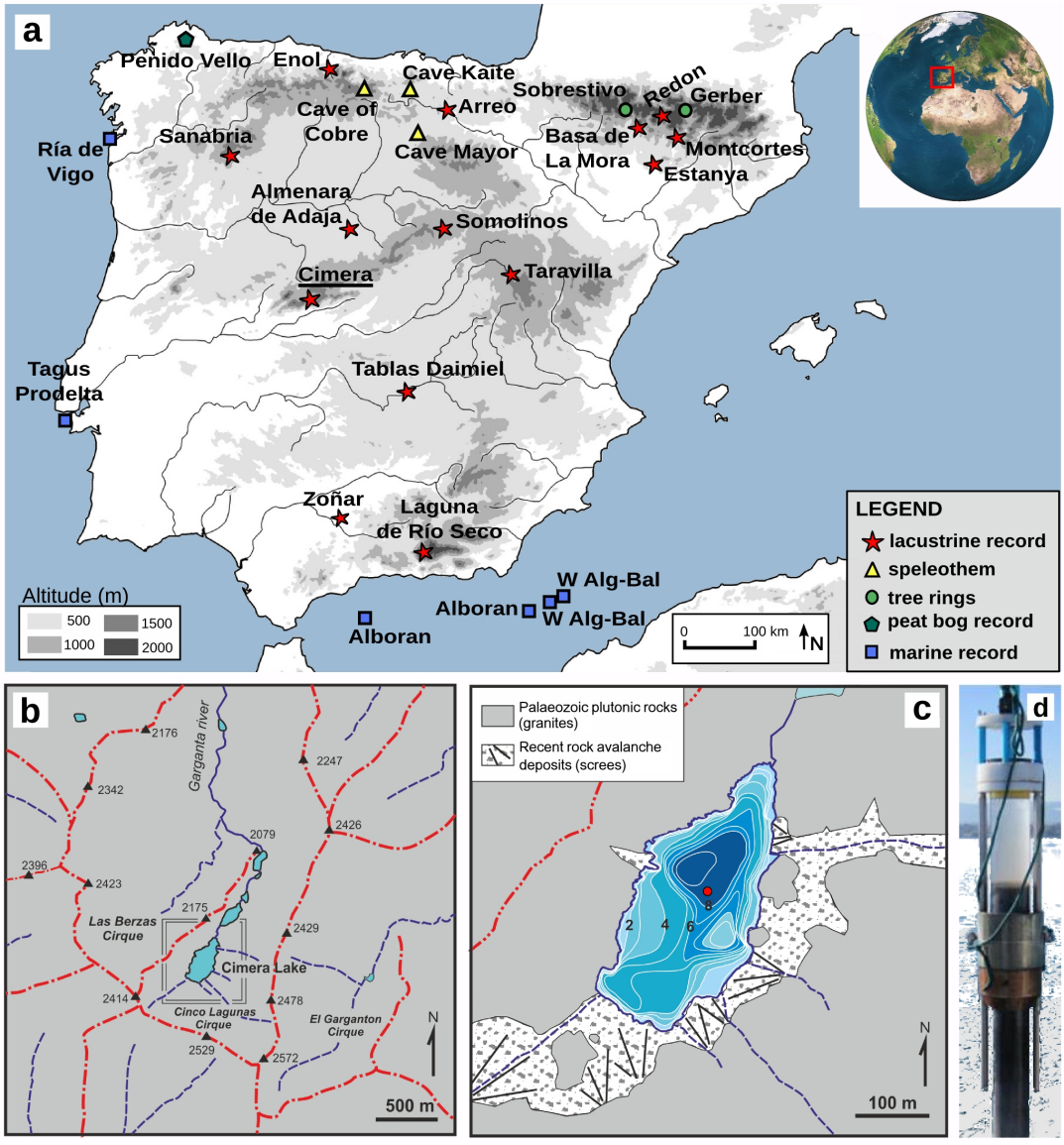

## 2.2.- Limnological setting

Cimera Lake (40°15'N - 5°18'W) is the highest (2140 m a.s.l.) of a series of 5 alpine lakes located in a glacial cirque of the Massif Central of *Sierra de Gredos* (Fig. 1b; Palacios et al., 2011). Cimera is a shallow lake (9.4 m maximum depth) with a small surface (5 ha, 384 m long, 177 m wide), and the catchment (75.6 ha) is primarily composed of exposed plutonic rock (granites) (Fig. 1c) and exhibits scarce developed soils and small grasslands and psychroxerophytic meadows (*Nardus* sp.) (Granados and Toro, 2000). The southern sector has a mean water depth of 5.5 m, and its sedimentation is dominated by coarse gravel scree deposits (Fig. 1c). There are two temporary stream inlets in the southern littoral of the lake and one outlet on the northern side that becomes dry in late summer (Fig. 1c; Granados and Toro, 2000). Flood currents from these streams are the origin of the major volume of fine sediment inputs accumulated in the offshore zone of the northern part of the lake. Cimera Lake is a discontinuous cold polymictic lake (Toro et al., 2006) that usually starts freezing between November and December, and it becomes completely ice-free in May-June (Sánchez-López et al., 2015). Cimera can also be classified as an oligotrophic lake because of the total mean phosphorus values (7 µg P-PO4 $l^{-1}$), maximum and mean annual chlorophyll values (11.5 µg Chl-a $l^{-1}$ and 2.1 µg Chl-a $l^{-1}$, respectively) and mean Secchi disk depth (5 m) (Catalan et al., 2002; Granados and Toro, 2000). The dissolved oxygen concentration in the water column has an annual periodic fluctuation (0-12 mg/l) and usually presents 80-120% oxygen saturation values during the open water period and intense bottom depletion in winter because of the thick ice cover. The lake water is slightly acidic (mean pH of 6.8) and exhibits low conductivity (<10 µS/cm at 25 °C) and nutrient contents (N and P) (Catalan et al. 2002; Granados and Toro, 2000).

# 3. MATERIALS AND METHODS

In winter 2012, ten sediment cores from Cimera Lake were retrieved using the UWITECE© gravity recovering system (Fig. 1d). All of the cores were sealed, transported to the laboratory, and then stored in a dark cool room at + 4 °C until sampling.

**3.1.- Sedimentary facies, geochemical and mineralogical analyses**

The sediment cores were split longitudinally into two halves, and after a visual lithological description, core CIM12-04A (124.8 cm long) was selected for this study as representative of the main offshore facies (Fig. 1c). Microscopic observations of smear slides were conducted every 5 cm and in the most relevant sedimentary layers to characterize these sedimentary facies.

The better preserved half of the CIM12-04A core was imaged with a colour line scan camera mounted in an X-Ray fluorescence (XRF) Avaatech core scanner at the University of Barcelona (Spain). This XRF core scanner was also employed to determine the chemical composition of the sediments under the following settings: 2 mm spatial resolution; 2 mA; 15 s count time and 10 kV for lighter elements; and 55 s count time and 30 kV for heavier elements. Thirty chemical elements were measured, although only ten lighter (Al, Si, K, Ca, Ti, V, Cr, Mn, Fe and Zn) and three heavier (Rb, Sr and Zr) elements had sufficient counts to be considered statistically consistent. Pearson's correlation analyses at two significance levels (1% and 5%) were conducted for the thirteen chemical elements to simplify the results by eliminating redundant information (Table S1). From the elements with highly significant correlations ($r>0.8$, p-value$<0.01$; Table S1), those with the largest number of counts (i.e., Si, Ti, V, Cr, Mn, Zn, Rb and Zr) were selected.

Table S1. Pearson's correlation coefficients among the elements obtained by XRF analyses. All of the correlations are significant at the 0.01 level except for the numbers in italics, which are significant at the 0.5 level, and the grey numbers, which do not indicate significant correlations; $n>340$.

| CIM12-04A | Al | Si | K | Ca | Ti | V | Cr | Mn | Fe | Zn | Rb | Sr | Zr |
|---|---|---|---|---|---|---|---|---|---|---|---|---|---|
| **Al** | 1 | | | | | | | | | | | | |
| **Si** | 0.99 | 1 | | | | | | | | | | | |
| **K** | 0.84 | 0.88 | 1 | | | | | | | | | | |
| **Ca** | 0.41 | 0.47 | 0.69 | 1 | | | | | | | | | |
| **Ti** | 0.69 | 0.74 | 0.94 | 0.79 | 1 | | | | | | | | |
| **V** | 0.31 | 0.34 | 0.5 | 0.54 | 0.59 | 1 | | | | | | | |
| **Cr** | 0.6 | 0.62 | 0.62 | 0.46 | 0.62 | 0.37 | 1 | | | | | | |
| **Mn** | 0.34 | 0.34 | 0.31 | 0.34 | 0.32 | 0.14 | 0.31 | 1 | | | | | |
| **Fe** | 0.52 | 0.59 | 0.84 | 0.69 | 0.92 | 0.58 | 0.54 | 0.19 | 1 | | | | |
| **Zn** | 0.23 | 0.26 | 0.4 | 0.63 | 0.55 | 0.38 | 0.37 | 0.4 | 0.53 | 1 | | | |
| **Rb** | 0.2 | 0.22 | 0.42 | 0.37 | 0.4 | 0.21 | *0.1* | -0.02 | 0.29 | 0.01 | 1 | | |
| **Sr** | 0.06 | 0.08 | 0.26 | 0.44 | 0.29 | 0.24 | 0.08 | 0 | 0.17 | 0.06 | 0.81 | 1 | |
| **Zr** | 0.13 | 0.17 | 0.41 | 0.53 | 0.56 | 0.38 | 0.27 | 0.18 | 0.58 | 0.57 | 0.24 | 0.18 | 1 |

The core was subsampled for the other proxies every 2 mm between depths of 0 and 36 cm and every 5 mm between depths of 36 and 124.8 cm. The different sampling resolutions were determined based on a previous chronological model (Granados and Toro, 2000). All of the samples were dried at 60 °C for 48 h and manually ground using an agate mortar.

Mineralogical analyses were conducted by X-ray diffraction (XRD) using a SIEMENS-D500 automatic X-ray diffractometer (Cu-Kα, 40 kV, 30 mA and graphite monochromator) at the Institute of Earth Sciences Jaume Almera (ICTJA-CSIC, Barcelona). The identification and quantification of the relative abundances of the different mineralogical species were conducted following the standard procedure (Chung, 1974a, 1974b).

The same samples employed for the XRD analysis were also used for the total carbon (TC), total nitrogen (TN) (RSD, 5% of the measurements), $\delta^{13}C$ and $\delta^{15}N$ analyses (0.2‰ analytical precision). These analyses were conducted using a Finnigan DELTAplus TC/EA-CF-IRMS spectrometer at the Centres Científics i Tecnològics of the Universitat de Barcelona (Barcelona). The carbonate content of the samples was below the detection

limit (<1%) of the XRD analysis; thus, the total carbon (TC) was considered equivalent to the total organic carbon (TOC).

### 3.2.- Age-depth model

The chronological framework of CIM12-04A was derived using the $^{210}$Pb activity-depth profile together with AMS $^{14}$C dating of terrestrial plant macroremains and pollen concentrates.

The concentration profile of $^{210}$Pb in the uppermost 20 cm of the core was determined by quantifying its decay product $^{210}$Po by alpha-spectroscopy following Sánchez-Cabeza et al. (1998). The supported $^{210}$Pb concentration was estimated by averaging the concentration of $^{210}$Pb below 9 cm, where it remained constant because there was not enough material available to conduct measurements by gamma spectrometry. $^{210}Pb_{ex}$-derived sediment accumulation rates were calculated by applying the constant flux: constant sedimentation model (CF:CS, Krishnaswamy et al., 1971). The pollen concentrates were obtained following Rull et al. (2010). Radiocarbon ages were calibrated to calendar years (BP and AD/BC) using the online CALIB 7.1 software (Stuiver and Reimer, 1993) and INTCAL13 curve (Reimer et al., 2013) by selecting the median of the 95.4% distribution (2σ probability interval) (Table 1). Finally, the age-depth relationship for the CIM12-04A model was established using the R-code package 'clam' and a smooth spline (type 4) with a 0.3 smoothing value and 1000 iterations (Blaauw, 2010).

Table 1. Radiocarbon dates and calibrated ages for the CIM12-04A core. Results are reported with 2σ uncertainty. Samples in italics were discarded.

| Depth (cm) | Lab Code | Material | $^{14}$C years BP | Cal. years BP (2σ) | Cal. years AD/BC (2σ) |
|---|---|---|---|---|---|
| *10* | *Beta - 333752* | *Pollen concentrate* | *1420 ± 30* | *1329 ± 39* | *621 ± 39 AD* |
| 29.5 | Poz-61896 | Pollen concentrate | 1140 ± 30 | 1032 ± 63 | 918 ± 63 AD |
| 49 | Beta - 333753 | Pollen concentrate | 1170± 30 | 1113 ± 66 | 837 ± 66 AD |

| | | | | | |
|---|---|---|---|---|---|
| 67.5 | Poz-61897 | Pollen concentrate | 1425 ± 30 | 1332 ± 40 | 618 ± 40 AD |
| 86 | Beta - 333754 | Pollen concentrate | 1940 ± 30 | 1885 ± 64.5 | 64.5 ± 64.5 AD |
| 105.5 | Poz-61898 | Pollen concentrate | 1875 ± 30 | 1803.5 ± 76.5 | 146.5 ± 76.5 AD |
| 124.5 | Beta - 333755 | Pollen concentrate | 2160 ± 30 | 2122.5 ± 65.5 | 172.5 ± 65.5 BC |

### 3.3.- Statistical analysis

The statistical treatment of the data was performed with R software (R Core Team, 2015) with the packages 'simecol' (Petzoldt and Rinke, 2007) and 'vegan' (Oksanen et al., 2013). XRF data were resampled with a regular spacing of 5 mm from 36 to 124.8 cm using the R function 'approxTime' to obtain the same spatial resolution to conduct the statistical analyses for all proxies.

A principal component analysis (PCA) was applied to the normalized geochemical datasets (i.e., XRF, TOC, TN, $\delta^{13}C$ and $\delta^{15}N$ data) to determine the main environmental processes that control the input, distribution and deposition of the sediments in the lake. A redundancy data analysis (RDA) was conducted between the geochemical (response) and mineralogical (explicative) datasets. The mineralogical composition of the sediment was used as a constraining matrix because each mineralogical species represents a 'compendium' of geochemical elements (Giralt et al., 2008). The RDA was used to establish the origin of the geochemical parameters and their relationships with the associated mineral phases.

## 4. RESULTS

### 4.1.- Sedimentary facies, geochemistry and mineralogy

Three sedimentary facies were identified in the CIM12-04A core (Fig. 2). Facies M1 is composed of massive brown silty mud with disperse grains of fine sand. Organic matter is present as predominant amorphous aggregates and a low content of altered terrestrial plant remains (i.e., phytoclasts). Facies M2 is characterized by poorly defined layers of

brown silty mud and fine to medium sand, the sand grain shape appears to be more angular than in facies M1, and there are amorphous aggregates of organic material, although in a lower proportion than in facies M1. Facies S is composed of white to ochre coarse sand with granules forming well-defined tabular layers, some of which include pebble clasts. Most of the grains show a more angular shape than those in facies M2, and the terrigenous fraction in facies S is significantly higher than the organic matter content. Facies M2 and S are characterized by maximum values of Rb (Fig. 2).

The TOC and TN contents display average values of approximately 3.5 and 0.35% wt., respectively. From the bottom to a depth of 6 cm, both parameters positively covary around their respective mean values (Fig. 2). Above this interval, the TOC and TN percentages largely increase until the top of the core. From the core bottom to a depth of 14.5 cm, the TOC/TN ratio remains constant at approximately 12. Subsequently, the TOC/TN ratio increases to approximately 14 in the 14.5 – 6.5 cm depth interval (Fig. 2). Above 6.5 cm, the ratio decreases to approximately 11, and a final sudden increase occurs at the top of the core (Fig. 2). The isotopic composition of this core shows $\delta^{13}C$ values between -25.5 and -24‰ and $\delta^{15}N$ values between 0 and 3‰ (Fig. 2). The $\delta^{13}C$ content displays an enrichment trend above 35 cm and a sudden depletion at the top of the core, whereas the $\delta^{15}N$ shows a noticeable depletion trend from 14.5 cm to the top of the core (Fig. 2). Si and Ti display the most remarkable oscillations, whereas V, Cr and Mn are the noisiest. The Mn profile decreases upwards, whereas Zr displays the opposite pattern. All of the inorganic elements show fewer counts in the uppermost centimetres (Fig. 2). The mineral species exhibit a roughly constant percentage from the core bottom to a depth of 35 cm. Above this interval, kaolinite and clinochlore increase, whereas quartz and microcline display the opposite trend (Fig. 2). Between 35 and 10 cm, muscovite diminishes from 29% to 24% wt., whereas albite remains constant. The uppermost 10 cm is characterized by an increase of muscovite and major oscillations of albite (Fig. 2).

Figure 2. Selected XRF profiles (expressed in counts per second and indicated by orange lines), elemental and isotopic compositions (TOC, TN, TOC/TN ratio are indicated by light-blue lines; $\delta^{13}C$ and $\delta^{15}N$ are indicated dark-blue lines), mineralogy (expressed as percentages of the total dry weight; Ms=muscovite, Kln=kaolinite, Clc=clinochlore, Qtz=quartz, Mc=microcline, Alb=albite; light-green lines correspond to the original data and dark-green lines correspond to the smoothed data calculated with the Loess function and a span degree=0.10), the first, second and third eigenvector ($PC1_{cim}$, $PC2_{cim}$ and $PC3_{cim}$, respectively) scores (black lines) and sedimentary facies of the CIM12-04A core. The main five climate periods are showed in the grey band (RP=Roman Period, EMA=Early Middle Ages, MCA=Medieval Climate Anomaly, LIA=Little Ice Age and Ind. Era=Industrial Era).

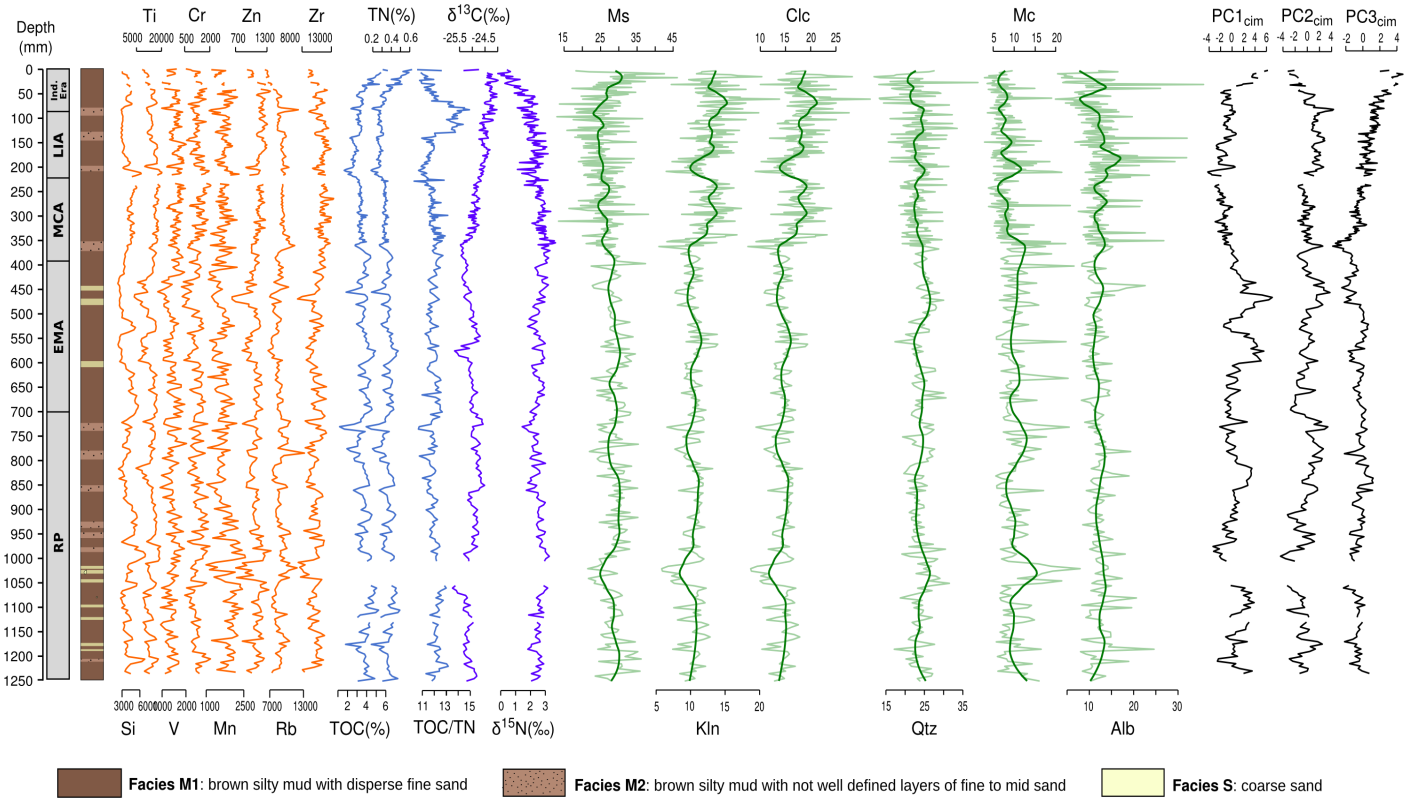

## 4.2.- Age-depth model

The concentration profile of the excess $^{210}Pb$ can be divided into three intervals according to its slopes: 0 - 4 cm, 4 - 6.5 cm and 6.5 - 9 cm. The supported $^{210}Pb$ horizon is attained at 9.2 cm. Relatively lower concentrations of $^{210}Pb_{ex}$ were measured in the sandy layers and excluded for the estimation of the sedimentation rates for each zone (Fig. 3). The sedimentation rates (SRs) were obtained by applying the CF:CS model. The concentration of $^{210}Pb_{ex}$ was constant in the 6.5 - 9 cm interval; thus, a chronology could not be derived.

Figure 3. Concentration profiles of the total and excess $^{210}Pb$ for the CIM12-04A core; error bars represent 1σ uncertainties.

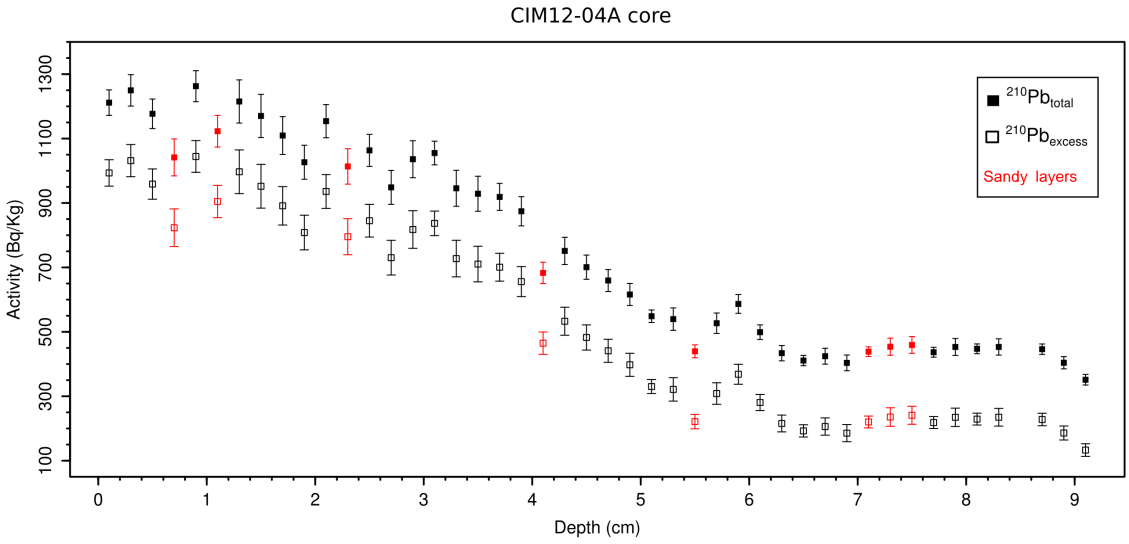


Seven AMS $^{14}C$ dates were determined between 10 and 124.5 cm (Table 1). All of the dates present a stratigraphical coherence except for the sample located at 10 cm because the age of this sample was too old for its stratigraphic location, which was most likely a result of the reworking of the older sediment. Therefore, this sample was not used in the construction of the age-depth model (Fig. 4).

Figure 4. Age-depth model based on the AMS $^{14}C$ dates and $^{210}Pb$ activity-depth profile.

Error bars for the red points represent the ±2 sigma calibrated age range for AMS $^{14}C$ dates. The black continuous line represents the age-depth function framed by the grey area, which corresponds to the error model. The blue dashed line represents the zone of $^{210}Pb$ dates.

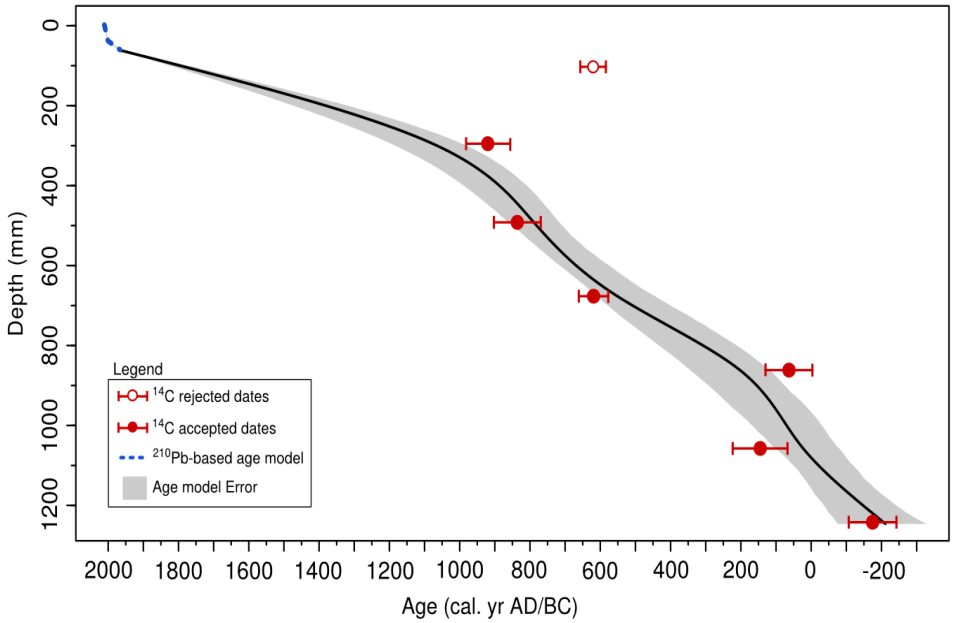


Four distinct SR intervals can be differentiated according to the age depth model: a) 4.1 mm/yr for 0 - 4 cm, b) 0.65 mm/yr for 4 - 6.5 cm, c) 0.2 mm/yr for 6.5 - 29.5 cm and d) 0.9 mm/yr for 29.5 – 124.5 cm. The SRs from the two first intervals were calculated by applying the CF:CS model, whereas the third and fourth intervals were obtained by linear interpolations between dates. The resulting age-depth model shows that the uppermost 124.5 cm of sedimentary infill spans from 172 ± 65 BC (2122 ± 65 BP) to 2012 AD (Fig. 4).

### 4.3.- Statistical analyses

#### 4.3.1. Redundancy analysis (RDA)

The RDA biplot allowed us to define three main groups (Fig. 5): group A includes Ti, Rb and $\delta^{15}N$ and is associated with quartz, albite and microcline; group B is associated with muscovite and the TOC and TN proportions; and group C includes Zn and $\delta^{13}C$ and is associated with kaolinite and clinochlore. Zr is located between group A and B, although

most of the geochemical elements (i.e., Si, Ti, V, Cr and Mn) are generally located in the centre of the biplot (Fig. 5).

Figure 5. (a) RDA biplot for the Cimera Lake record. Light red, grey and yellow areas indicate groups A, B and C, respectively. (b, c, d) PCA biplots showing the first, second and third eigenvectors for the Cimera Lake record.

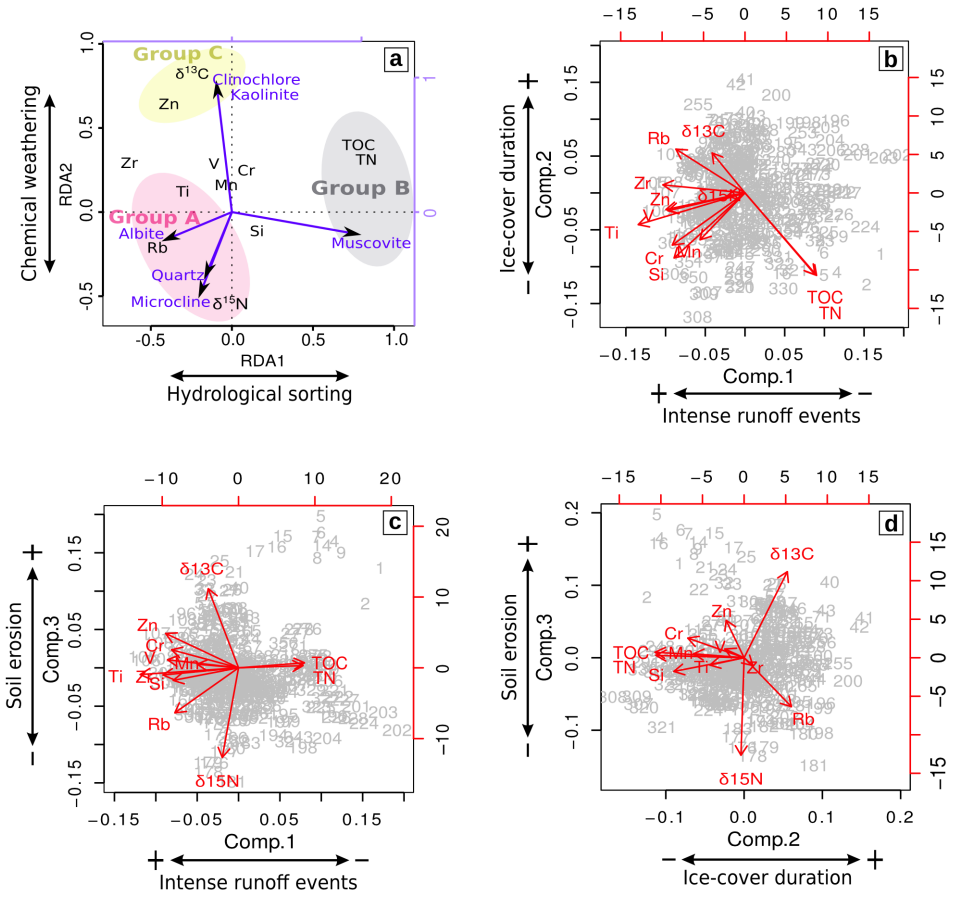


### 4.3.2. Principal component analysis (PCA)

The PCA of the geochemical dataset shows that the first three eigenvectors account for 67% of the total variance (Table 2a). The first eigenvector ($PC1_{cim}$) explains 34% of the total variance and is primarily controlled by Ti and the remaining geochemical elements (to a lesser extent) at the negative end and by the TOC and TN percentages at the positive end (Table 2 and Fig. 5). The second eigenvector ($PC2_{cim}$) represents 18.5% of the total

variance and is mainly controlled by the presence of TOC, TN and most of the geochemical elements at the negative end and by Rb and $\delta^{13}C$ at the positive end (Table 2 and Fig. 5). The third eigenvector ($PC3_{cim}$) accounts for 14.31% of the total variance and is mostly controlled by $\delta^{13}C$ at the positive end and by $\delta^{15}N$ at the negative end (Table 2 and Fig. 5). The other eigenvectors defined by the PCA analysis were not considered because they explain considerably lower percentages of the total variance (Table 2).

Table 2. Principal component analysis (PCA). (a) Eigenvalues for the twelve obtained components. The percentage of the variance explained and the cumulative percentage for every axis are also shown. (b) Factor loads for every variable in the three main axes from PCA. The hyphens correspond to loadings <0.1.

(a)

| Component | Initial eigenvalues | | |
|---|---|---|---|
| | Total | % of variance | % Cumulative |
| 1 | 2.01 | 33.81 | 33.81 |
| 2 | 1.49 | 18.51 | 52.32 |
| 3 | 1.31 | 14.31 | 66.63 |
| 4 | 0.98 | 7.97 | 74.6 |
| 5 | 0.93 | 7.24 | 81.84 |
| 6 | 0.75 | 4.72 | 86.56 |
| 7 | 0.67 | 3.7 | 90.26 |
| 8 | 0.63 | 3.27 | 93.53 |
| 9 | 0.61 | 3.07 | 96.6 |
| 10 | 0.53 | 2.32 | 98.92 |
| 11 | 0.32 | 0.86 | 99.78 |
| 12 | 0.17 | 0.23 | 100 |

(b)

| | Component | | |
|---|---|---|---|
| | 1 | 2 | 3 |
| TOC | 0.29 | -0.49 | - |
| TN | 0.30 | -0.50 | - |
| $\delta^{13}C$ | -0.14 | 0.24 | 0.59 |
| $\delta^{15}N$ | - | - | -0.66 |
| Si | -0.29 | -0.39 | - |
| Ti | -0.44 | -0.19 | - |
| V | -0.32 | -0.11 | - |
| Cr | -0.30 | -0.31 | 0.13 |
| Mn | -0.19 | -0.28 | - |
| Zn | -0.33 | - | 0.26 |
| Rb | -0.29 | 0.26 | -0.33 |
| Zr | -0.34 | - | - |

## 5. DISCUSSION

### 5.1.- Sedimentology and interpretation of statistical analyses (RDA and PCA)

The RDA analysis shows that elements such as Ti, Zr and Rb can be used as

389 indicators of physico-chemical processes (Fig. 5a). The association of these elements with
390 coarse material from the granites (i.e., quartz, albite and microcline) and their lack of
391 association with fine material (i.e., muscovite) related to the organic content suggests that
392 the first RDA eigenvector can be interpreted in terms of the hydrological sorting of
393 siliciclastic inputs (Fig. 5a).

394 The $PC1_{cim}$ is associated with most of the chemical elements and Ti in particular
395 (Figs. 5b and 5c and Table 2), and it is derived from detrital minerals that are not affected
396 by diagenetic processes. Therefore, the lack of association between these detrital
397 elements and the organic matter content suggests that the $PC1_{cim}$ reflects changes in the
398 inputs of siliciclastic material from the catchment. Negative (positive) values of the first
399 eigenvector indicate higher (lower) siliciclastic inputs with a major (minor) presence of
400 coarse material (Fig. 5). Hence, higher siliciclastic inputs imply lower hydrological sorting
401 because of fine and coarse detrital material entering the lake and vice versa. These
402 coarser siliciclastic inputs lead to the dilution of the in-lake organic matter production,
403 thereby reducing its percentages in the deposited lake sediments, whereas fine siliciclastic
404 material inputs (i.e., muscovite) cause the opposite conditions. In alpine lakes, one of the
405 main transport processes governing siliciclastic inputs is runoff derived from snowmelt.
406 The intensity of the runoff is controlled by the occurrence of a well-defined melt season in
407 terms of temperature and rainfall variations (Pelto, 2008). Hence, during periods
408 characterized by warmer springs caused by an earlier increase of temperature, the
409 snowmelt coincides with the arrival of spring rainfalls, thereby leading to rain-on-snow
410 events, which are responsible for intense runoff episodes (Asikainen et al., 2006; Nesje et
411 al., 2001; Parris et al., 2010; Fig. 6). These higher runoff energy currents reduce the
412 hydrological sorting and increase the proportion of coarse-grained material from less
413 weathered parent rock (i.e., quartz, albite and microcline) in the sediments. However,
414 during periods characterized by later increases of temperature, a portion of the spring

precipitation occurs in the form of snow, which reduces the rain-on-snow events and diminishes the possibility of extreme runoff currents (Fig. 6). The gradual snow melt with a lower runoff energy transport then enhances the hydrological sorting and increases the proportion of fine material (i.e., muscovite mud grains) in the sediments.

Figure 6. Diagram explaining the meteorological winter-spring conditions that determine the occurrence or not of rain-on-snow events. The black dashed lines correspond to a temperature of 0 °C, and red lines represent the temperature evolution.

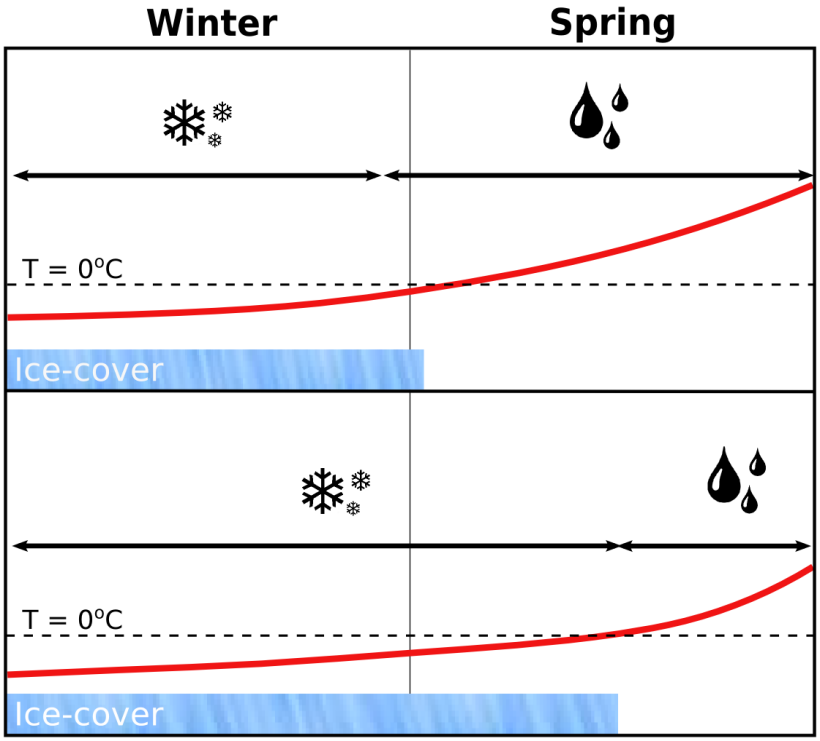


Although rain-on-snow events are among the main processes governing the inputs of coarse material to Cimera Lake, summer and autumn storms may also represent an important factor that controls the inputs of siliciclastic material. Hence, it can be hypothesized that certain sandy M2 and S facies layers might correspond to high-energy flood events derived from these storms (Fig. 2).

The second eigenvector of the RDA analysis opposes Rb, associated with unaltered

siliciclastic material (i.e., quartz, albite and microcline), to Zn, related with weathered minerals (i.e., kaolinite and clinochlore) that are partially associated with the organic fraction (Fig. 5a). This analysis also shows that $\delta^{13}C$ enrichments are linked to increases in the proportion of chemically weathered material and $\delta^{15}N$ depletions are associated with decreases of coarse-grained unaltered material (Figs. 2 and 5). Hence, this eigenvector can be interpreted in terms of the chemical weathering of the granites present in the soil catchment.

The $PC2_{cim}$ is mostly related to the TOC, TN and Rb values (Figs. 5b and 5d and Table 2). The TOC concentration is a bulk value that represents the fraction of organic matter that escaped remineralization during sedimentation, and it is commonly considered a good indicator of the organic productivity of a lake (Meyers and Teranes, 2001). The burial of organic matter is frequently followed by the rapid loss of N (Cohen, 2003), and the positive covariance of the two proxies indicate negligible organic matter degradation. In addition, the TOC/TN ratio, which presented values of approximately 13 (Fig. 2), suggests that the accumulated organic matter has a mainly algal origin (Meyers and Lallier-Vergès, 1999). Therefore, the $PC2_{cim}$ is associated with variations in the lake organic productivity. Positive (negative) values of the second eigenvector represent a decrease (increase) in lake productivity associated with both the internal recycling of nutrients and inputs of weathered material from the catchment (to a lesser extent). The weathered material is produced by a series of chemical reactions that occur in soils (Catalan et al., 2014) and generate a pool of micronutrients that when released by soil erosion, might enhance the in-lake productivity. In alpine lakes, the ice-cover duration modulates lake productivity through its influence on the growing season length and summer stratification as well as the lake overturning strength and timing, which determines the internal lake nutrient cycle (Catalan and Fee, 1994; Catalan et al., 2002; Pla-Rabes and Catalan, 2011). The ice cover of Iberian alpine lakes depends on both the winter-spring temperature and

accumulated precipitation in the form of snow on the ice cover. Cold (warm) and wet (dry) conditions will lead to longer (shorter) ice-cover durations, which is partly a result of the enhanced (reduced) insulating effect of the snow deposited on the ice cover (Sánchez-López et al., 2015). Therefore, during periods characterized by colder spring temperatures and a prolonged snow season, the ice cover will last longer (Fig. 6), which will lead to a shorter growing season and thus lower lake productivity. However, the opposite situation occurs during periods characterized by shorter ice-cover durations as a result of warmer spring temperatures and a shorter snow season (Fig. 6).

The interpretation of the $PC3_{cim}$ is related to variations in the isotopic composition (i.e., $\delta^{13}C$ and $\delta^{15}N$) of the organic matter (Figs. 5c and 5d). Because the RDA eigenvector has been previously interpreted in terms of the inputs of weathered material produced in soils, the $PC3_{cim}$ could be a rough indicator of soil erosion. Neither of the isotopic signatures shows a trend from the bottom to a depth of 35 cm in the studied core. Above this interval, there is a $\delta^{13}C$ enrichment and a $\delta^{15}N$ depletion, with the latter change more prominent in the uppermost 7.5 cm of the sequence (Fig. 2). These variations coincide with remarkable increases in the contents of clay minerals (Fig. 2). The TOC/TN ratio increases between 22.5 cm and 7.5 cm, and together with the $\delta^{13}C$ fluctuations located between 35 and 7.5 cm, it may be related to inputs of organic matter from the erosion of the catchment soil (Meyers and Lallier-Vergès, 1999; Meyers and Teranes, 2001). The soil organic matter is usually $\delta^{13}C$ enriched because of remineralization and $\delta^{15}N$ depleted because of its atmospheric origin (Meyers and Teranes, 2001). Therefore, the supply of this organic matter to the lake might explain the variations of the isotope records. The positive covariance between the $PC3_{cim}$ and the increased clay mineral proportions would also support the soil erosion hypothesis (Fig. 2).

However, in the uppermost 7.5 cm, the TOC and TN percentages increase significantly and the $\delta^{15}N$ depletion is more prominent (Fig. 2), and these changes could be

related to global climate change (Catalan et al., 2013). The lake productivity could have been enhanced because of temperature increases and large inputs of atmospheric nitrogen ($\delta^{15}N$ depleted) resulting from increments of the global pool of reactive nitrogen (Bergstrom and Jansson, 2006). Fossil fuel combustion and the Haber-Bosch process have altered the global nitrogen cycle (Galloway and Cowling, 2002). A large number of sediment records from remote lakes in the Northern Hemisphere also show this $\delta^{15}N$ depletion during the Industrial Era (Hastings et al., 2009; Holtgrieve et al., 2011). The enhancement of the chemical weathering over a short time scale because of the present global warming trend (Catalan et al., 2014) might also intensify the biogeochemical reactions within the lake, thereby contributing to the observed increases in TOC and TN and decreases in the TOC/TN ratio during the Industrial Era. Hence, the $PC3_{cim}$ in this last interval could provide an indicator of the effects of global warming and/or human pollution, which could have similar effects on $\delta^{15}N$ because of the organic matter inputs derived from soil erosion.

In summary, from the bottom to a depth of 7.5 cm in the Cimera sequence, positive values of the $PC3_{cim}$ reflect an enhancement of soil erosion episodes, whereas in the uppermost 7.5 cm, this eigenvector might also reflect the influence of global warming and/or human pollution on lake productivity.

**5.2.- Climatic and environmental changes in the ICR and IP over the last two millennia**

The multivariate analyses of the geochemical and mineralogical datasets from the Cimera record (Fig. 7) and comparisons with the main IP sedimentary records (Fig. 8) were used to establish the contextual climatic and environmental conditions over the last two millennia in the IP. This reconstruction includes five main climate chronozones.

Figure 7. Variations of $PC1_{cim}$, $PC2_{cim}$ and $PC3_{cim}$ scores relative to age in the Cimera Lake sequence. Main climate periods are indicated with grey dashed lines. Original data are plotted in grey lines and smoothed data calculated with the Loess function and a span degree=0.10 are represented by thicker black lines. Vertical bars correspond to thermal and hydrological conditions suggested by the processes assigned to $PC1_{cim}$ and $PC2_{cim}$. Figure

8. Summary of the climatic conditions reconstructed from different records in the Iberian Peninsula (IP). A=arid, H=humid, C=cold, and W=warm, and arrows indicate climate transitions. Fig. 1a shows the locations of these records. The records from the northern to southern IP include the Penido Vello peat bog (Martínez-Cortizas et al., 1999); Ría de Vigo (Desprat et al., 2003; Álvarez et al., 2005); Sanabria Lake (Jambrina-Enriquez et al., 2014); Enol (Moreno et al., 2011); Cobre, Kaite and Mayor caves (Martín-Chivelet et al., 2011); Arreo Lake (Corella et al., 2013); Estanya Lake (Morellón et al. 2009, 2011); Montcortès Lake (Corella et al., 2011); Basa de la Mora Lake (1914 m; Moreno et al., 2012; Pérez-Sanz et al., 2013); Redon Lake (Pla and Catalan, 2005, 2011; Catalan et al., 2009); Sobrestribo and Gerber tree rings (Büntgen et al., 2008); Almenara de Adaja (López-Merino et al. 2009); Somolinos tufa lake (Currás et al., 2012); Cimera Lake (this study); Taravilla Lake (Moreno et al., 2008); Tablas de Daimiel wetland (Gil García et al., 2007); Tagus Prodelta (Abrantes et al. 2005; Rodrigues et al., 2009); Zoñar Lake (Martín-Puertas et al., 2008); Laguna de Río Seco (Jiménez-Espejo et al., 2014); Alboran sea (Martín-Puertas et al., 2010); and West Algerian-Balearic sea (Nieto-Moreno et al. 2011).

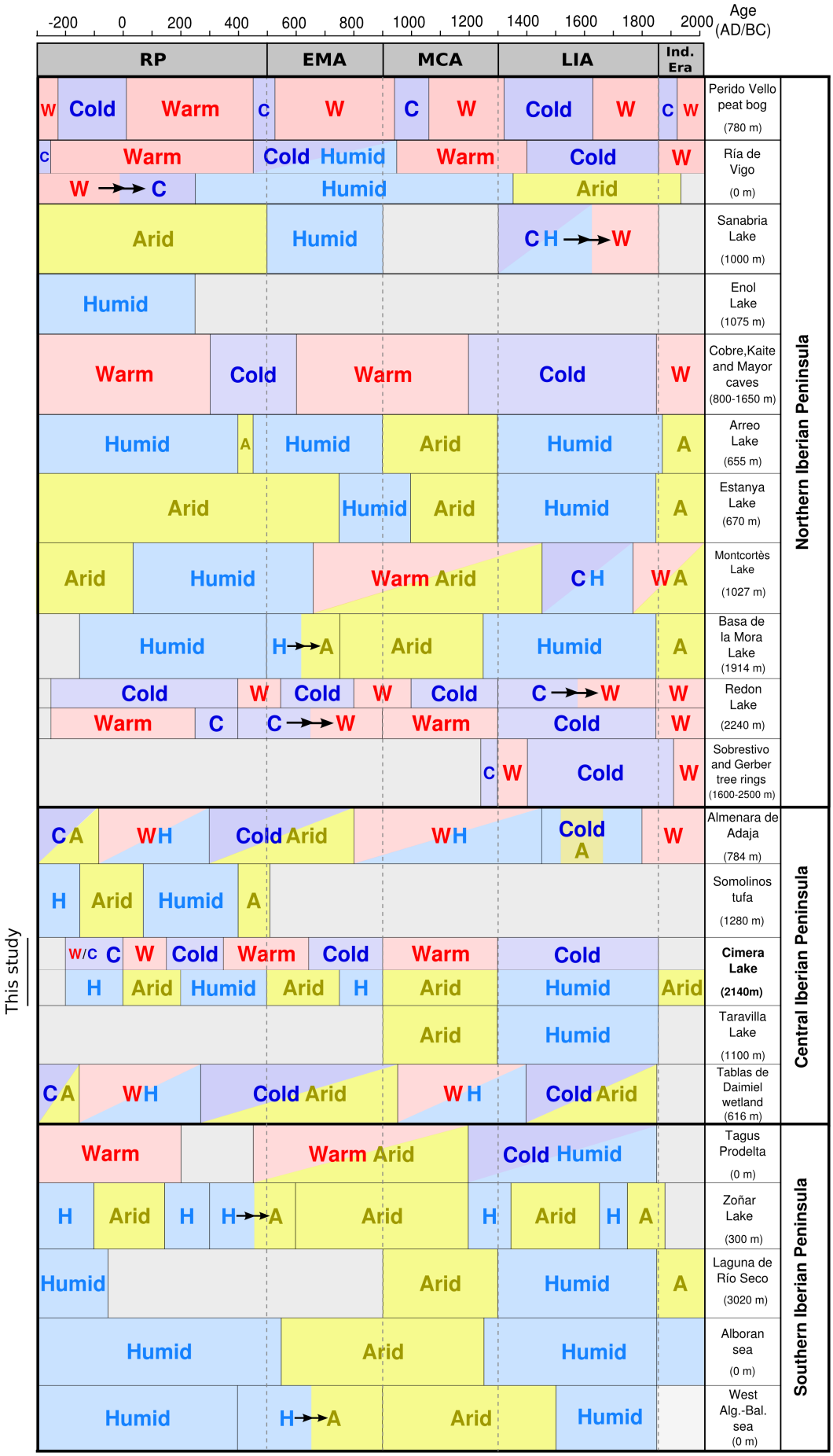
-200
0
200
400
600
800
1000
1200
1400
1600
1800
2000
Age (AD/BC)
RP
EMA
MCA
LIA
Ind. Era
This study
Perido Vello peat bog (780 m)
Ría de Vigo (0 m)
Sanabria Lake (1000 m)
Enol Lake (1075 m)
Cobre,Kaite and Mayor caves (800-1650 m)
Arreo Lake (655 m)
Estanya Lake (670 m)
Montcortès Lake (1027 m)
Basa de la Mora Lake (1914 m)
Redon Lake (2240 m)
Sobrestivo and Gerber tree rings (1600-2500 m)
Almenara de Adaja (784 m)
Somolinos tufa (1280 m)
Cimera Lake (2140m)
Taravilla Lake (1100 m)
Tablas de Daimiel wetland (616 m)
Tagus Prodelta (0 m)
Zoñar Lake (300 m)
Laguna de Río Seco (3020 m)
Alboran sea (0 m)
West Alg.-Bal. sea (0 m)
Northern Iberian Peninsula
Central Iberian Peninsula
Southern Iberian Peninsula

*Roman Period (~250 BC – 500 AD)*

In terms of thermal conditions, the sedimentary records from the NW of the IP indicate predominantly warm conditions during this period (Álvarez et al., 2005; Desprat et al., 2003; Martín-Chivelet et al., 2011; Martínez-Cortizas et al., 1999). In the Pyrenees, Redon Lake displayed low winter-spring temperatures (~200 BC – 400 AD) and a warming trend at the end (Pla and Catalan, 2005, 2011), whereas the summer-autumn temperatures showed a transition from cold to warm conditions (Catalan et al., 2009). In the centre of the IP, Almenara de Adaja (López-Merino et al., 2009) and Tablas de Daimiel (Gil García et al., 2007) registered a centennial scale alternation of cold and warm periods, whereas the Cimera Lake sequence exhibited decadal short-lived periods of rain-on-snow events, which suggest cold and warm oscillations (Fig. 7 and 8). These differences in the frequency of climatic oscillations can be partially ascribed to the lower temporal resolution of the first Iberian records. Finally, the Tagus Prodelta recorded a warm period (Abrantes et al. 2005; Rodrigues et al., 2009). To our knowledge records from the southern IP have not been employer in temperature reconstructions.

In terms of humidity, the northwestern IP presented an arid phase that was observed in the marine and lacustrine records (Bernárdez et al., 2008; Jambrina-Enríquez et al., 2014), although towards the east, Enol Lake showed the opposite conditions (Moreno et al., 2011). In the Pyrenees, Estanya Lake displayed a dry climate scenario (Morellón et al., 2009), whereas the remaining records (Arreo, Montcortès and Basa de la Mora Lakes) displayed large increases in water availability (Corella et al., 2011, 2013; Pérez-Sanz et al., 2013). In the Central IP, all of the records showed an alternation between arid and humid phases (Currás et al., 2012; García et al., 2007; López-Merino et al., 2009). Cimera Lake showed multidecadal alternations of long and short ice-cover durations derived from variations of lake productivity (Fig. 7 and 8) resulting from fluctuations between periods of longer winter snow seasons during colder and/or wetter conditions and opposite condi-

557 tions. These multidecadal alternations led to periodic oscillations in soil erosion (Fig. 7). In
558 addition, the presence of S and M2 facies (Fig. 2) might be associated with frequent au-
559 tumn/summer storms in this region. In the southern IP and western Mediterranean region,
560 the marine (Alboran Sea and west Algerian-Balearic Basin) and terrestrial records (Zoñar
561 Lake) displayed prevalent wet conditions (Martín-Puertas et al., 2008, 2010; Nieto-Moreno
562 et al., 2011).

563 Therefore, during the RP, the northern IP was characterized by a W–E longitudinal
564 gradient in terms of humidity (Fig. 8), with humid conditions prevailing at higher altitudes
565 towards the eastern areas and dry conditions prevailing at lower altitudes towards the
566 western areas. A broad N–S humidity gradient also occurred, with humid conditions gener-
567 ally occurring in the southern part of the IP and dominant arid conditions occurring in the
568 northern part (Fig. 8). These W–E and N–S humidity gradients highlight the complex inter-
569 play between geography, topography and climate.

570 *Early Middle Ages (500 – 900 AD)*

571 General humid and cold conditions were registered by the marine and lacustrine re-
572 cords in the NW IP (Álvarez et al., 2005; Desprat et al., 2003; Jambrina-Enríquez et al.,
573 2014). However, spatial heterogeneity was also observed as indicated by the predomin-
574 antly warm temperatures of the Penido Vello peat bog (Martínez-Cortizas et al., 1999) and
575 speleothem records from the Cobre, Mayior and Kaite caves (Martín-Chivelet et al., 2011)
576 (Fig. 8). In the Pyrenees, the records showed a strong disparity in humidity, with Arreo
577 Lake displaying wet conditions caused by less saline conditions and high lake levels (Co-
578 rella et al., 2013; Moreno et al., 2011) and Estanya Lake presenting a dominant dry scen-
579 ario between 500 and 750 AD (Morellón et al., 2009). Montcortès and Basa de la Mora
580 lakes displayed a shift from humid to arid conditions (Corella et al., 2011; Pérez-Sanz et
581 al., 2013). In terms of the thermal conditions in the Pyrenees, the summer-autumn temper-
582 atures in Redon Lake exhibited a transition from cold to warm temperatures (Catalan et al.,

583 2009), whereas the winter-spring temperatures remained cold (Pla and Catalan, 2005,
584 2011). In the central IP, the Almenara de Adaja (López-Merino et al., 2009) and Tablas de
585 Daimiel (Gil García et al., 2007) records registered a cold and arid EMA, although the first
586 record indicated the opposite conditions at the end of this period. Between 500 and 630
587 AD, Cimera Lake was characterized by more rain-on-snow events and shorter ice covers
588 as reflected in enhanced lake productivity, which suggested warm temperatures and arid
589 conditions and shorter snow seasons, whereas from 630 to 900 AD, the Cimera Lake re-
590 cord presented the opposite conditions (Figs. 7 and 8). These long-term climate conditions
591 may also indicate a progressive inhibition of soil erosion in Cimera Lake. The low fre-
592 quency of S facies (Fig. 2) is consistent with the low floods observed in the Tagus River
593 basin during this climate period (Benito et al., 2003a, 2003b). In the southern IP and west-
594 ern Mediterranean region, the marine and terrestrial records displayed a trend towards
595 drier conditions (Martín-Puertas et al., 2008, 2010; Nieto-Moreno et al., 2011).

596 Therefore, the E–W humidity gradient only occurred in the northern IP, and pro-
597 gressively more arid conditions occurred westward. Nevertheless, the N–S humidity gradi-
598 ent affected the entire IP and produced generally humid conditions in the northern area, a
599 transition from arid to humid conditions in the ICR, and a dry scenario in the southern area
600 (Fig. 8). The progressive increase in humidity in the ICR suggests a southwards displace-
601 ment of this humidity gradient over time.

602 *Medieval Climate Anomaly (900 – 1300 AD)*

603 Moreno et al. (2012) conducted a comprehensive characterization of the MCA cli-
604 mate evolution for the IP and showed that the selected continental records from the Medi-
605 terranean IP generally registered drier conditions as indicated by lower water levels and
606 higher chemical concentrations. Marine cores also indicated a decrease in the fluvial sup-
607 ply and an increase in Saharan dust particles. Records from the NW IP indicated an in-
608 crease in humidity during the MCA, which reflects the opposite behaviour to that of the

609 Mediterranean IP. Thus, Morellón et al. (2012) focused on the available climatic evidence
610 from the Pyrenees and concluded that warmer and more arid conditions prevailed during
611 the MCA in this region as evidenced by lower lake levels, decreased runoff and a signific-
612 ant development of xerophytes and Mediterranean vegetation. The only climate recon-
613 struction that presented an opposite behaviour was that for Redon Lake, and the opposite
614 behaviour might have be related to the combination of multiple local factors, such as the
615 geographical location and orientation (Morellón et al., 2012).

616 Climate records that were not included in the previous reviews suggest that high
617 temperatures occurred in the northern IP (Martín-Chivelet et al., 2011) and arid conditions
618 occurred in the south IP (Martín-Puertas et al., 2010) (Fig. 8). In the ICR, the Cimera Lake
619 record displayed a predominant warm and arid scenario as indicated by the prevalent rain-
620 on-snow events and an increasing trend of lake productivity caused by short ice covers re-
621 lated to the shorter snow season (Fig. 7). Furthermore, the development and weathering of
622 soils in the Cimera Lake catchment caused by these optimal climatic conditions favoured
623 soil erosion, which is indicated by a marked increasing trend in erosion (Fig. 7). The
624 scarce presence of M2 facies (Fig. 2) might be associated with a minor frequency of au-
625 tumn/summer storms in the ICR. Benito et al. (2003a) found that large flood events de-
626 creased in the Tagus River basin during the period 1205 –1450 AD, which might partially
627 support our hypothesis.

628 The integration of the previous works with these new climate records (Fig. 8) indic-
629 ates that although wet conditions were recorded in the marine records from the northwest
630 end of the IP, arid and dry conditions were mostly predominant throughout the entire IP
631 (Moreno et al., 2012). Thus, compared with the conditions during the RP and EMA, an
632 evident N–S or E–W humid gradient did not occur during the MCA.

633 *Little Ice Age (1300 – 1850 AD)*

Morellón et al. (2012) also included a detailed reconstruction of the main climate changes during the LIA in the Pyrenees, and to the best of our knowledge, additional comprehensive LIA evolutions for the entire IP are not available.

Northern Iberian records consistently show that the onset of the LIA registered cold and humid climate conditions that progressively became warmer. Only the Ría de Vigo record displays arid conditions (Álvarez et al., 2005; Desprat et al., 2003). In the Pyrenees, Morellón et al. (2012) demonstrated that cold and humid conditions with higher lake levels and increased runoff prevailed during this period. All of the records in the mid-latitudes of the IP recorded cold conditions, although they displayed differences in terms of humidity, with Taravilla Lake (Moreno et al., 2008) and Tagus Prodelta (Abrantes et al., 2005; Rodrigues et al., 2009) showing predominantly wet conditions and Almenara de Adaja (López-Merino et al., 2009) and Tablas de Daimiel (Gil García et al., 2007) displaying predominantly arid conditions (Fig. 8). The Cimera Lake record was characterized by a decreasing trend of intense runoff events and prevalent low lake productivity with decadal oscillations, which indicated predominant long ice-cover durations caused by prolonged snow seasons (Fig. 7). These conditions on the ICR were likely provoked by a colder period with dry-wet-dry decadal oscillations within the framework of a general humid scenario (Fig. 8). This climatic scenario was broadly reflected in the Cimera Lake soil erosion, which was generally constant and likely caused by cold conditions disfavouring the development and disintegration of soils (Fig. 7). The high frequency of M2 facies (Fig. 2) might also indicate the major presence of autumn/summer storms in the ICR, which was also observed for the Tagus River (Benito et al., 2003a, 2003b). Finally, in the southern IP and western Mediterranean, humid conditions with a decadal oscillating pattern were observed (Martín-Puertas et al., 2010; Nieto-Moreno et al., 2011). The generalized low lake productivity shown in the central and southern Iberian records (Jiménez-Espejo et al., 2014; Martín-Puertas et al.,

2008) may be explained by the dominant humid conditions that prevailed during the LIA and likely inhibited the deposition of nutrient inputs from northern African dust.

Therefore, despite minor discrepancies, prevalent wet and cold climatic conditions were recorded throughout the entire IP (Fig. 8).

*Industrial Era (1850 - 2012 AD)*

The records included in this study show that over the last 150 years, the IP has been characterized by predominant warm and arid conditions (Fig. 8), which are most likely associated with the current global warming trend. Nevertheless, the intensification of human activities during the Industrial Era and their impact on natural ecosystems have increased the difficulty of discerning and evaluating climate signals (Fig. 8).

The Cimera Lake sequence showed an increasing trend of lake productivity that was partially triggered by progressively shorter ice-cover durations, which were likely caused by less prolonged snow seasons and suggest prevalent arid conditions in the ICR (Fig. 7). However, between 1850 and 1950 AD, the Cimera sequence presented a shift from a minor to major frequency of intense runoff episodes, whereas over the last 50 years, the sequence displayed a marked decrease in these episodes. These environmental conditions suggest an earlier warming and a rapid shift to cold conditions over the last decades. These colder conditions for the last 50 years clearly contradict the current global warming scenario. Granados and Toro (2000) indicated that the Cimera Lake summer water has warmed by more than 1.5 °C since the 1980s, which is consistent with the rise of temperatures caused by global warming. The $PC3_{cim}$ might also reflect the influence of global warming in Cimera Lake. An explanation for this apparent contradiction may be found in the rapid increase of organic matter (i.e., TOC and TN) in the sediments. This increase in the proportion of organic matter most likely has diluted the inorganic fraction of the sediments, thereby lowering the signal of almost all XRF geochemical elements (Fig. 2).

### 5.3.- Climate-forcing mechanisms driving climate variability in the IP over the last two millennia

The climate evolution of the IP over the last 2000 years indicates that two spatiotemporal climate patterns have occurred. During the RP and EMA periods, W–E and N–S humidity gradients co-occurred, whereas during the MCA and LIA, these climate gradients were not observed (Fig. 8).

The NAO has been shown to represent the climate mode responsible for the largest share of the climate variability in the North Atlantic and European regions in recent decades (Hurrell et al., 2003). Thus, the majority of Iberian climate reconstructions over the last 1000 years have attributed most of the observed climate variability to variations in the NAO (e.g., Morellón et al., 2012; Moreno et al., 2012; Nieto-Moreno et al., 2011). These climate reconstructions commonly ascribe the warm and arid climate conditions of the MCA to the dominant positive phases of the NAO and the humid and cold conditions of the LIA to the predominance of negative phases of the NAO (Ortega et al., 2015; Trouet et al., 2009).

Nevertheless, as initially stated, several recent works suggest that other North Atlantic climate modes, such as the East Atlantic (EA) and Scandinavian (SCAND) patterns, significantly influence most climate variables in Europe (Comas-Bru and McDermott, 2014; Jerez and Trigo, 2013). Furthermore, the influence of the combined influence of the NAO and EA over Europe has been extended to vegetation dynamics and carbon uptake (Bastos et al., 2016) and to precipitation dynamics and the $\delta^{18}O$–NAO relationship (Comas-Bru et al., 2016).

EA and SCAND modulate variations in the strength and location of the NAO dipoles at the multidecadal scale (Comas-Bru and McDermott, 2014). The combined influence of the NAO–EA and NAO–SCAND leads to shifts in the winter temperature and precipitation anomaly patterns in Western Europe (Comas-Bru and McDermott, 2014). When the NAO

711 and EA modes have the same sign, the precipitation and temperature patterns present a
712 homogeneous spatial distribution, whereas when these modes have the opposite sign, the
713 precipitation and temperature patterns present heterogeneous spatial distributions (Bastos
714 et al., 2016; Comas-Bru and McDermott, 2014) (Fig. 9). In the IP, Hernández et al. (2015)
715 showed that the NAO mainly governs winter precipitation and the EA governs winter and
716 summer temperatures. These authors also showed that the Iberian lake dynamics are
717 sensitive to the seasonal effects of interannual variations in these three patterns.
718
719 Figure 9. Spearman correlation coefficients showing the spatial coherence of the NAO–cli-
720 mate relationship (i.e., wPre and wTmp) and the authors' EOF-based indices (i.e., NAO
721 and EA) for different combinations of signs: (a) and (b) modes in the same phase (NAO–
722 EA)$_S$; n=57; (c) and (d) modes in opposite phases (NAO–EA)$_O$; n=51. Precipitation and
723 temperature (wPre and wTmp) datasets for boreal winters (December–February) between
724 1902 and 2009 were calculated using the CRU-TS3.1 global climate dataset. Reprinted
725 from Comas-Bru and McDermott (2014) with permission from Wiley.

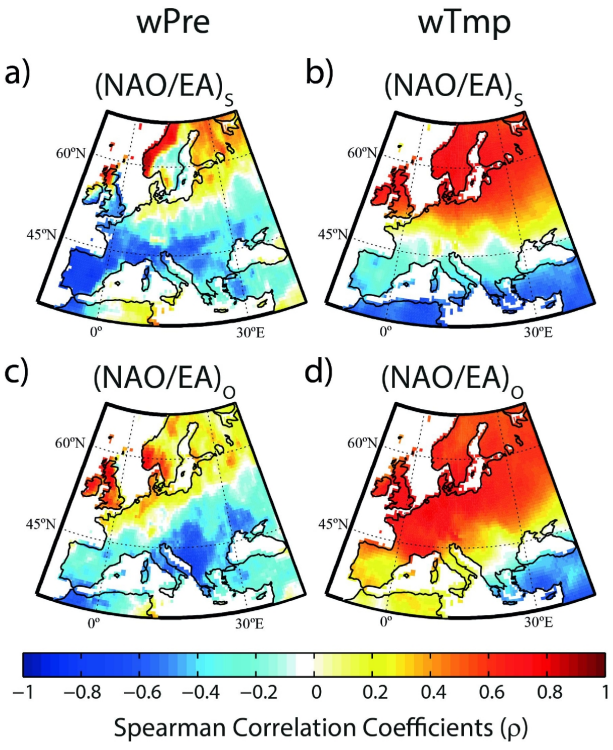

The role of these other climate modes and their interactions could explain the spatiotemporal climate variability observed in the IP over the last millennia. The humidity gradients recognized during the RP and EMA periods in the IP might have been caused by a predominant coincidence of the NAO and EA in opposite phases ($NAO^{+}$–$EA^{-}$ or $NAO^{-}$–$EA^{+}$) (Fig. 9). The thermal conditions and the humidity gradients present during the RP suggest that the prevalent climate was dominated by the phase combination $NAO^{-}$–$EA^{+}$, which Hernández et al. (2015) indicated led to wet and warm winters and warm summers (Fig. 8). Conversely, the EMA presented an arid gradient with generally cold conditions, which suggests that the $NAO^{+}$–$EA^{-}$ combination dominated the main climate variability and led to dry and cold winters and cold summers (Fig. 8).

However, the homogeneous climate spatial conditions that dominated the MCA and LIA might have also been caused by a predominance of both climate modes acting in the same phase (Fig. 9). Thus, the MCA would be marked by a predominance of the positive phases of the NAO and EA ($NAO^{+}$–$EA^{+}$), which would lead to dry and warm winters and warm summers, whereas the LIA would be dominated by the opposite phases ($NAO^{-}$–$EA^{-}$) of these climate modes, which would lead to cold and wet winters and cold summers (Fig. 8).

The relationship between climate (e.g., NAO) and external climatic forcings, such as volcanic and solar forcings (e.g., in the frequency domain), is a controversial theme because of their complex relationships (Mann, 2007; Sigl et al., 2015; Stoffel et al., 2015). Despite this complex relationship, predominant NAO and EA phases during the RP, EMA, MCA and LIA appear to be associated with a large-scale dynamic response of the climate system to explosive volcanic and solar forcings. Therefore, during the RP and MCA, the solar irradiance was relatively high and there were few explosive tropical volcanic eruptions, whereas during the EMA and LIA, the solar irradiance was characterized by several periods of solar minima and there were more frequent tropical volcanic eruptions (Table 3;

753 Sigl et al., 2015; Steinhilber et al., 2009). These forcings might have modulated the NAO
754 and EA phases over the last two millennia (Table 3). Most of the climate reconstructions for
755 the last millennium have assumed a linear relationship between the solar activity and the
756 NAO because other climate modes have not been considered (Morellón et al., 2012).
757 However, our results suggest that at the multidecadal scale, the solar activity fluctuations
758 would be reflected in the EA.

759

760 Table 3. Frequency of tropical volcanic eruptions from Sigl et al. (2015), intensity of solar
761 irradiance forcing obtained from Steinhilber et al. (2009), and presence of blocking events
762 and ocean and continent conditions ascribed to the forcings, NAO and EA phases and
763 general climate conditions over the Iberian Peninsula during the RP, EMA, MCA and LIA
764 climate periods.

765

| Climate period | RP | EMA | MCA | LIA |
|---|---|---|---|---|
| Tropical volcanic eruptions | - | + | - | + |
| Solar irradiance forcing | high | low | high | low |
| Blocking events frequency | low | high | low | high |
| Ocean and continent conditions during blocking events | --- | Cold ocean<br>Warm continent | --- | Warm ocean<br>Cold continent |
| EA phase | + | - | + | - |
| NAO phase | - | + | + | - |
| General climate conditions over Iberian Peninsula | Wet and warm winters and warm summers | Dry and cold winters and cold summers | Dry and warm winters and warm summers | Wet and cold winters and cold summers |

766

767 Another consequence of the relationship between solar activity and climate modes
768 is the development of atmospheric blocking events, which consist of a quasi-stationary
769 high-pressure system in the eastern North Atlantic region that modifies the flow of the
770 westerly winds (Barriopedro et al., 2008; Trigo et al., 2004). Low solar irradiance promotes
771 the development of frequent and persistent atmospheric blocking events (Moffa-Sánchez

et al., 2014). These blocking events usually last a sufficiently long time (i.e., between 1 and 3 weeks) to induce significant climate anomalies over a wide area of Europe (Trigo et al., 2004), although the occurrence of these anomalies is dependent on the location (Sousa et al., 2015). The position, frequency and persistence of these blocking events on the central North Atlantic Ocean are mainly conditioned by the phase of the NAO (Shabbar et al., 2001). The $NAO^+$ leads to a ‘cold ocean/warm land’ pattern, which is unfavourable for the development and persistence of blocking events, whereas the $NAO^-$ phase leads to a ‘warm ocean/cold land’ pattern, which promotes the formation and persistence of blocks (Shabbar et al., 2001). Recently, the location and persistence of these blocking events over the eastern North Atlantic has also been associated with the phase of the EA pattern (Moffa-Sánchez et al., 2014).

During the EMA and LIA (Moffa-Sánchez et al., 2014), low solar irradiance promoted the development of frequent and persistent atmospheric blocking events. The dominance of $EA^-$ climate phase conditions during these two climate periods suggests that blocking events developed on the North Atlantic Ocean (Table 3). However, the NAO phase of these climate periods determined the main humidity and thermal dominance conditions. The $NAO^+$ phase dominated the EMA and led to a 'cold ocean/warm land' pattern (Shabbar et al., 2001), which inhibited ocean water evaporation. This pattern together with the low-frequency and less persistent blocking events generally led to arid and relatively cold conditions in the IP (Table 3). Conversely, the LIA was governed by a $NAO^-$ phase that led to a 'warm ocean/cold land' pattern (Shabbar et al., 2001), which enhanced the ocean water evaporation. This second pattern together with high-frequency and persistent blocks promoted a general humid and cold scenario during this period (Table 3).

## 6. CONCLUSIONS

The Cimera Lake sequence has provided valuable insights into the climatic and environmental conditions of the ICR for the last two millennia. Geochemical and mineralogical datasets revealed that climatic conditions were transmitted to the sediments via the frequency of intense runoff episodes caused by rain-on-snow events as well as the lake productivity, which was primarily governed by the ice-cover duration. The soil erosion within the catchment also broadly supported these climatic variations. The onset of the RP (200 BC – 350 AD) exhibited multidecadal oscillations in the frequency of intense runoff events resulting from the alternation between cold and warm intervals. From the second half of the RP (350 – 500 AD) to the onset of the EMA (500 – 650 AD), an increase in the frequency of these unusually intense runoff episodes indicated the dominance of warm conditions, whereas a pronounced decrease during the rest of the EMA (650 – 900 AD) suggested a shift to a cold scenario. These long-term climate conditions were also reflected in a progressive reduction in soil erosion. Both the RP and EMA climate periods displayed a long-term decrease in lake productivity as demonstrated by a transition from arid to humid conditions. The MCA (900 – 1300 AD) was characterized by a predominant warm and dry scenario as indicated by an increase in exceptionally intense runoff episodes, high lake productivity and soil erosion, whereas the LIA (1300 – 1850 AD) presented the opposite climate conditions. The Industrial Era (1850 – 2012 AD) showed a noticeable increase of lake productivity because of short ice-cover durations, which were likely a consequence of global warming.

By compiling the main Iberian climate reconstructions and integrating new data from the Cimera Lake, we were able to perform a detailed spatiotemporal climatic reconstruction for the last two millennia. The discrepancies found during the RP (200 BC – 500 AD) and EMA (500 – 900 AD) periods indicated the occurrence of humidity gradients. The RP in the northern IP exhibited a W–E gradient, with prevailing humid conditions at higher altitudes eastwards and drier conditions at lower altitudes westwards. The predominant

arid conditions in the northern IP and generally humid conditions in the southern IP also indicated a broad N–S gradient during this period. The EMA also displayed an E–W humidity gradient in the northern IP, with progressively arid conditions occurring westward. Furthermore, a N–S humidity gradient affected the entire IP during this period and caused generally humid conditions in the northern area, a transition from arid to humid conditions in the ICR, and a dry scenario in the southern area. However, homogeneous spatial climate conditions dominated the MCA (900 – 1300 AD) and LIA (900 – 1300 AD), with a prevalent warm and arid scenario characterizing the MCA and a cold and wet scenario characterizing the LIA.

Different interplays between the NAO and East Atlantic EA phases explain the climatic conditions and their spatial differences during each period. The general warm conditions and humidity gradients during the RP suggest a predominance of the $NAO^-$–$EA^+$ interplay, whereas the opposite climatic conditions during the EMA suggest $NAO^+$–$EA^-$ interactions. The dominant warm and arid conditions during the MCA and the cold and humid conditions during the LIA indicate $NAO^+$–$EA^+$ and $NAO^-$–$EA^-$ interactions, respectively. Additionally, the high solar irradiance and fewer tropical volcanic eruptions during the RP and MCA might reinforce the hypothesis of a predominant $EA^+$ phase during these periods. The opposite scenario during the EMA and LIA (i.e., low solar irradiance and more tropical volcanic eruptions) might indicate a predominance of the $EA^-$ phase, which would promote the formation of frequent and persistent atmospheric blocking events in the Atlantic region during these periods.

**Acknowledgements**

This work was financed by the Spanish Ministry of Economy and Competitiveness through the PALEONAO project (CGL2010-15767/BTE), the RapidNAO project (CGL2013-40608-R) and a PhD JAE grant (BOE 03/02/2011) to Guiomar Sánchez from the Spanish

National Research Council (CSIC). We thank the 'Servicio Territorial de Medio Ambiente de Ávila' of 'Junta de Castilla y León' for permitting the field work.

## References

Abrantes, F., Lebreiro, S., Rodrigues, T., Gil, I., Bartels-Jónsdóttir, H., Oliveira, P., Kissel, C., Grimalt, J.O., 2005. Shallow-marine sediment cores record climate variability and earthquake activity off Lisbon (Portugal) for the last 2000 years. Quat. Sci. Rev. 24, 2477–2494.

Agustí-Panareda, A., Thompson, R., 2002. Reconstructing air temperature at eleven remote alpine and Arctic lakes in Europe from 1781 to 1997 AD. J. Paleolimnol. 28, 7–23.

Álvarez, M.C., Flores, J.A., Sierro, F.J., Diz, P., Francés, G., Pelejero, C., Grimalt, J., 2005. Millennial surface water dynamics in the Ría de Vigo during the last 3000 years as revealed by coccoliths and molecular biomarkers. Palaeogeogr. Palaeoclimatol. Palaeoecol. 218, 1–13. doi:10.1016/j.palaeo.2004.12.002.

Asikainen, C.A., Francus, P., Brigham-Grette, J., 2006. Sedimentology, clay mineralogy and grain-size as indicators of 65 ka of climate change from El'gygytgyn Crater Lake, Northeastern Siberia. J. Paleolimnol. 37, 105–122.

Barreiro-Lostres, F., Brown, E., Moreno, A., Morellón, M., Abbott, M., Hillman, A., Giralt, S., Valero-Garcés, B., 2015. Sediment delivery and lake dynamics in a Mediterranean mountain watershed: human-climate interactions during the last millennium (El Tobar lake record, Iberian range, Spain). Sci. Total Environ. 533, 506–519.

Barriopedro, D., García-Herrera, R., Huth, R., 2008. Solar modulation of Northern hemisphere winter blocking. J. Geophys. Res. 113, D14118. doi:10.1029/2008JD009789.

Barry, R.G., Chorley, R.J., 2009. Atmosphere,Weather and Climate, ninth ed.. Routledge, London.

Bastos, A., Janssens, I.A., Gouveia, C.M., Trigo, R.M., Ciais, P., Chevallier, F., Peñuelas, J., Rödenbeck, C., Piao, S., Friedlingstein, P., Running, S.W., 2016. European land CO2 sink influenced by NAO and east-Atlantic pattern coupling. Nat. Commun. 7, 10315 doi:10.1038/ncomms10315.

Benito, G., Diéz-Herrero, A., Fernández de Villalta, M., 2003b. Magnitude and frequency of flooding in the Tagus Basin (Central Spain) over the last millennium. Clim. Change 58, 171–192.

Benito, G., Sopeña, A., Sánchez-Moya, Y., Machado, M.J., Pérez-González, A., 2003a. Palaeoflood record of the Tagus River (Central Spain) during the late Pleistocene and Holocene. Quat. Sci. Rev. 22, 1737–1756.

Bergstrom, A., Jansson, M., 2006. Atmospheric nitrogen deposition has caused nitrogen enrichment and eutrophication of lakes in the northern hemisphere. Glob. Change Biol. 12, 635-643.

Bernárdez, P., González-Álvarez, R., Francés, G., Prego, R., Bárcena, M.A., Romero, O.E., 2008. Late Holocene history of the rainfall in the NW Iberian peninsula – evidence from a marine record. J. Mar. Syst. 72, 366–382.

Blaauw, M., 2010. Methods and code for ‘classical’ age-modelling of radiocarbon sequences. Quat. Geochronology 5, 512–518.

Büntgen, U., Frank, D., Grudd, H., Esper, J., 2008. Long-term summer temperature variations in the Pyrenees. Clim. Dyn. 31, 615–631.

Castro-Díez, Y., Pozo-Vázquez, D., Rodrigo, F.S., Esteban-Parra, M.J., 2002. NAO and winter temperature variability in southern Europe. Geophys. Res. Lett. 29, 1160. doi:10.1029/2001GL014042.

Catalan, J., Fee, E.J., 1994. Interanual variability in limnic ecosystems: origin, patterns and predictability, in: Margalef, R. (Ed.), Limnology Now: A Paradigm of Planetary Problems.

Elsewier Science, New York, pp. 81–97.
Catalan, J., Pla, S., García, J., Camarero, L., 2009. Climate and CO2 saturation in an alpine lake throughout the Holocene. Limnol. Oceangr. 54, 2542–2552.
Catalan, J., Pla-Rabés, S., García, J., Camarero, L., 2014. Air temperature-driven CO2 consumption by rock weathering at short timescales: evidence from a Holocene lake sediment record. Geochim. Cosmochim. Acta 136, 67–79.
Catalan, J., Pla-Rabés, S., Wolfe, A.P., Smol, J.P., Rühland, K.M., Anderson, N.J., Kopáček, J., Stuchlík, E., Schmidt, R., Koinig, K.A., Camarero, L., Flower, R.J., Heiri, O., Kamenik, C., Korhola, A., Leavitt, P.R., Psenner, R., Renberg, I., 2013. Global change revealed by palaeolimnological records from remote lakes: a review. J. Paleolimnol. 49, 513–535.
Catalan, J., Ventura, M., Brancelj, A., Granados, I., Thies, H., Nickus, U., Korhola, A., Lotter, A.F., Barbieri, A., Stuchlík., E., Lien., L., Bitušík., P., Buchaca, T., Camarero, L., Goudsmit, G.H., Kopáćek, J., Lemcke, G., Livingstone, D.M., Müller, B., Rautio, M., Sisko, M., Sorvari, S., Sporka, F., Strunecky, O., Toro, M., 2002. Seasonal ecosystem variability in remote mountain lakes: implications for detecting climatic signals in sediment records. J. Paleolimnol. 28, 25–46.
Chung, F.H., 1974a. Quantitative interpretation of X-ray diffraction patterns of mixtures. I. Matrix-flushing method for quantitative multicomponent analysis. J. Appl. Crystallogr. 7, 519–525.
Chung, F.H., 1974b. Quantitative interpretation of X-ray diffraction patterns of mixtures. II. Adiabatic principle of X-ray diffraction analysis of mixtures. J. Appl. Crystallogr. 7, 526–531.
Cohen, A.S., 2003. Paleolimnology: the History and Evolution of Lake Systems. Oxford University, Press, p. 528.
Comas-Bru, L., McDermott, F., 2014. Impacts of the EA and SCA patterns on the European twentieth century NAO-winter climate relationship. Q. J. Roy. Meteorol. Soc. 140, 354–363.
Comas-Bru, L., McDermott, F., Werner, M., 2016.The effect of the east Atlantic pattern on the precipitation $\delta^{18}$O-NAO relationship in Europe. Clim. Dyn. 1, 1–11. doi:10.1007/s00382-015-2950-1.
Corella, J.P., Moreno, A., Morellón, M., Rull, V., Giralt, S., Rico, M.T., Pérez-Sanz, A., Valero-Garcés, B.L., 2011. Climate and human impact on a meromictic lake during the last 6,000 years (Montcortès Lake, Central Pyrenees, Spain). J. Paleolimnol. 46, 351–367.
Corella, J.P., Stefanova, V., El Anjoumi, A., Rico, E., Giralt, S., Moreno, A., Plata-Montero, A., Valero-Garcés, B.L., 2013. A 2500-year multi-proxy reconstruction of climate change and human activities in northern Spain: the lake Arreo record. Palaeogeogr., Palaeoclimatol., Palaeoecol. 386, 555–568.
Currás, A., Zamora, L., Reed, J.M., García-Soto, E., Ferrero, S., Armengol, X., Mezquita-Joanes, F., Marqués, M.A., Riera, S., Julià, R., 2012. Climate change and human impact in central Spain during Roman times: high-resolution multi-proxy analysis of a tufa lake record (Somolinos, 1280 m asl). Catena 89, 31–53.
De Vicente, G., González, J.M., Calvo, J.P., Muñoz, A., Giner, J., Rodríguez, M., 1994. Evolución y estructuras alpinas en la zona del centro Peninsular, vol. 19. Cadernos do Laboratorio Xeolóxico de Laxe, pp. 175–190.
Desprat, S., Sanchez Goñi, M.F., Loutre, M., 2003. Revealing climatic variability of the last three millennia in northwestern Iberia using pollen influx data. Earth Planet. Sci. Lett. 213, 63–78.
Durán, L., Sánchez, E., Yagüe, C., 2013. Climatology of precipitation over the Iberian Central System mountain range. Int. J. Climatol. 33, 2260–2273.
Galloway, J.N., Cowling, E.B., 2002. Reactive nitrogen and the world: 200 years of change. Am.Bio. 31, 64-71.
Gil García, M.J., Ruiz Zapata, M.B., Santisteban, J.I., Mediavilla, R., López-Pamo, E., Dabrio, C.J., 2007. Late Holocene environments in Las Tablas de Daimiel (south central Iberian peninsula, Spain). Veg. Hist. Archaeobotany 16, 241–250. doi:10.1007/s00334-006-0047-9.

Giralt, S., Moreno, A., Bao, R., Sáez, A., Prego, R., Valero-Garcés, B.L., Pueyo, J.J., González-Sampériz, P., Taberner, C., 2008. A statistical approach to disentangle environmental forcings in a lacustrine record: the Lago Chungara case (Chilean Altiplano). J. Paleolimnol. 40, 195–215.

Granados, I., Toro, M., 2000. Recent warming in a High Mountain Lake (Laguna Cimera, Central Spain) inferred by means of fossil chironomids. J. Limnol. 59, 109–119.

Hastings, M.G., Jarvis, J.C., Steig, E.J., 2009. Anthropogenic impacts on nitrogen isotopes of ice-core nitrate. Science 324, 1288. doi:10.1126/science.1170510.

Hernández, A., Trigo, R.M., Pla-Rabes, S., Valero-Garcés, B.L., Jerez, S., Rico-Herrero, M., Vega, J.C., Jambrina-Enríquez, M., Giralt, S., 2015. Sensitivity of two Iberian lakes to north Atlantic atmospheric circulation modes. Clim. Dyn. 45, 3403–3417. doi:10.1007/s00382-015-2547-8.

Holtgrieve, G.W., Schindler, D.E., Hobbs, W.O., Leavitt, P.R., Ward, E.J., Bunting, L., Chen,G., Finney, B.P., Gregory-Eaves, I., Holmgren, S., Lisac, M.J., Lisi, P.J., Nydick, K., Rogers, L.A., Saros, J.E., Selbie, D.T., Shapley, M.D., Walsh, P.B., Wolfe, A.P., 2011. A coherent signature of anthropogenic nitrogen deposition to remote watersheds of the northern hemisphere. Science 334, 1545–1548. doi:10.1126/science.1212267.

Hurrell, J.W., 1995. Decadal trends in the north Atlantic oscillation: regional temperatures and precipitation. Science 269, 676–679.

Hurrell, J.W., Kushnir, Y., Ottersen, G., Visbeck, M., 2003. An overview of the north Atlantic oscillation, in: Hurrell, J.W., Kushir, Y., Ottersen, G., Visbeck, M. (Eds.), The North Atlantic Oscillation, Climatic Significance and Environmental Impact. American Geophysical Union, Washington. Geophysical Monograph 134, pp 1–35.

Jambrina-Enríquez, M., Rico, M., Moreno, A., Leira, M., Bernárdez, P., Prego, R., Recio, C., Valero-Garcés, B.L., 2014. Timing of deglaciation and postglacial environmental dynamics in NW Iberia: the Sanabria Lake record. Quat. Sci. Rev. 94, 136–158.

Jerez, S., Trigo, R.M., 2013. Time-scale and extent at which large-scale circulation modes determine the wind and solar potential in the Iberian Peninsula. Environ. Res. Lett. 8, 044035.

Jiménez-Espejo, F.J., García-Alix, A., Jiménez-Moreno, G., Rodrigo-Gámiz, M., Anderson, R.S., Rodríguez-Tovar, F.J., Martínez-Ruiz, F., Giralt, S., Delgado Huertas, A., Pardo-Igúzquiza, E., 2014. Saharan aeolian input and effective humidity variations over Western Europe during the Holocene from a high altitude record. Chem. Geol. 374–375, 1–12. doi:10.1016/j.chemgeo.2014.03.001.

Krishnaswamy, S., Lal, D., Martin, J.M., Meybeck, M., 1971. Geochronology of lake sediments. Earth Planet. Science Lett. 11, 407–414.

Lionello, P. (Ed.), 2012. The Climate of the Mediterranean Region, From the past to the Future. Elsevier, Amsterdam, Netherlands, p. 502. ISBN: 9780124160422.

López-Merino, L., López-Sáez, J.A., Sánchez, F.A., Pérez-Díaz, S., Shaad, D.A., Guerra Doce, E., 2009. Estudio polínico de una Laguna endorreica en Almenara de Adaja (Valladolid, meseta Norte): cambios ambientales y actividad humana durante los últimos 2800 años. Revista Española de Micropaleontología 41, 333–348.

López-Sáez, J.A., Abel-Schaad, D., Pérez-Díaz, S., Blanco-González, A., Alba-Sánchez, F., Dorado, M., Ruiz-Zapata, M.B., Gil-García, M.J., Gómez-González, C., Franco-Múgica, F., 2014. Vegetation history, climate and human impact in the Spanish Central System over the last 9,000 years. Quat. Int. 353, 98–122. doi:10.1016/j.quaint.2013.06.034.

Luterbacher, J., Werner, J.P., Smerdon, J.E., Fernández-Donado, L., González-Rouco, F.J., Barriopedro, D., Ljungqvist, F.C., Büntgen, U., Zorita, E., Wagner, S., Esper, J., McCarroll, D., Toreti, A., Frank, D., Jungclaus, J.H., Barriendos, M., Bertolin, C., Bothe, O., Brázdil, R., Camuffo, D., 2016. European summer temperatures since Roman times. Environ. Res.

Lett. 11, 024001. doi:10.1088/1748-9326/11/1/02400.

Mann, M.E., 2007. Climate over the past two millennia. Annu. Rev. Earth Planet. Sci. 35, 111–136.

Martín-Chivelet, J., Muñoz-García, M.B., Edwards, L.R., Turrero, M.M., Ortega, A.I., 2011. Land surface temperature changes in Northern Iberia since 4000 yr BP, based on $\delta^{13}C$ of speleothems. Global Planet. Change 77, 1–12.

Martínez-Cortizas, A., Pontevedra-Pombal, X., García-Rodeja, E., Novoa-Munoz, J.C., Shotyk, W., 1999. Mercury in a Spanish Peat Bog: archive of climate change and atmospheric metal deposition. Science 284, 939–942. doi:10.1126/ science.284.5416.939.

Martín-Puertas, C., Jiménez-Espejo, F., Martínez-Ruiz, F., Nieto-Moreno, V., Rodrigo, M., Mata, M.P., Valero-Garcés, B.L., 2010. Late Holocene climate variability in the southwestern Mediterranean region: an integrated marine and terrestrial geochemical approach. Clim. Past 6, 807–816.

Martín-Puertas, C., Valero-Garcés, B.L., Pilar Mata, M., González-Sampériz, P., Bao, R., Moreno, A., Stefanova, V., 2008. Arid and humid phases in southern Spain during the last 4000 years: the Zoñar Lake record, Córdoba. Holocene 18, 907–921.

Meyers, P.A., Lallier-Vergès, E., 1999. Lacustrine sedimentary organic matter records of late quaternary paleoclimates. J. Paleolimnol. 21, 345–372. doi:10.1023/A:1008073732192.

Meyers, P.A., Teranes, J.L., 2001. Sediment organic matter, in: Last, W.M., Smol, J.P. (Eds.), Tracking Environmental Changes Using Lake Sediment, vol. 2: Physical and Geochemical Methods .Kluwer Academic Publishing House, Dordrecht, pp. 239–270.

Moffa-Sánchez, P., Born, A., Hall, I.R., Thornalley, D.J.R., Barker, S., 2014. Solar forcing of north Atlantic surface temperature and salinity over the past millennium. Nat. Geosci. 7, 275-278.

Morellón, M., Pérez-Sanz, A., Corella, J.P., Büntgen, U., Catalán, J., González-Sampériz, P., González-Trueba, J.J., López-Sáez, J.A., Moreno, A., Pla-Rabes, S., Saz-Sánchez, M.A., Scussolini, P., Serrano, E., Steinhilber, F., Stefanova, V., Vegas-Vilarrúbia, T., Valero-Garcés, B., 2012. A multi-proxy perspective on millennium-long climate variability in the southern Pyrenees. Clim. Past 8, 683–700.

Morellón, M., Valero-Garcés, B., González-Sampériz, P., Vegas-Vilarrúbia, T., Rubio, E., Rieradevall, M., Delgado-Huertas, A., Mata, P., Romero, Ó., Engstrom, D.R., López-Vicente, M., Navas, A., Soto, J., 2011. Climate changes and human activities recorded in the sediments of Lake Estanya (NE Spain) during the Medieval Warm Period and Little Ice Age. J. Paleolimnol. 46, 423–452.

Morellón, M., Valero-Garcés, B., Vegas-Vilarrúbia, T., González-Sampériz, P., Romero, Ó., Delgado-Huertas, A., Mata, P., Moreno, A., Rico, M., Corella, J.P., 2009. Lateglacial and Holocene palaeohydrology in the western Mediterranean region: the lake Estanya record (NE Spain). Quat. Sci. Rev. 28, 2582–2599.

Moreno, A., López-Merino, L., Leira, M., Marco-Barba, J., González-Sampériz, P., Valero-Garcés, B.L., López-Sáez, J.A., Santos, L., Mata, P., Ito, E., 2011. Revealing the last 13,500 years of environmental history from the multiproxy record of a mountain lake (Lago Enol, northern Iberian Peninsula). J. Paleolimnol. 46, 327–349.

Moreno, A., Pérez, A., Frigola, J., Nieto-Moreno, V., Rodrigo-Gámiz, M., Martrat, B., González-Sampériz, P., Morellón, M., Martín-Puertas, C., Corella, J.P., Belmonte, Á, Sancho, C., Cacho, I., Herrera, G., Canals, M., Grimalt, J.O., Jiménez-Espejo, F., Martínez-Ruiz, F., Vegas-Vilarrúbia, T., Valero-Garcés, B.L., 2012. The medieval climate anomaly in the Iberian Peninsula reconstructed from marine and lake records. Quat. Sci. Rev. 43, 16–32.

Moreno, A., Valero-Garcés, B.L., González-Sampériz, P., Rico, M., 2008. Flood response to rainfall variability during the last 2000 years inferred from the Taravilla Lake record (Central Iberian range, Spain). J. Paleolimnol. 40, 943–961.

Nesje, A., Dahl, S.O., Matthews, J.A., Berrisford, M.S., 2001. A ~ 4500-yr record of river floods obtained from a sediment core in lake Atnsjoen, eastern Norway. J. Paleolimnol. 25, 329–

342.
Nieto-Moreno, V., Martínez-Ruiz, F., Giralt, S., Jiménez -Espejo, F., Gallego-Torres, D., Rodrigo-Gámiz, M., García -Orellana, J., Ortega-Huertas, M., de Lange, G.J., 2011. Tracking climate variability in the Western Mediterranean during the Late Holocene: a multiproxy approach. Clim. Past 7, 1395–1414.
Ninyerola, M., Pons, X., Roure, J.M., 2005. Atlas Climático Digital de la Península Ibérica. Metodología y Aplicaciones en Bioclimatología y Geobotánica. Universidad Autónoma de Barcelona, Bellaterra.
Oksanen, J., Guillaume Blanchet, F., Kindt, R., Legendre, P., Minchin, P.R., O'Hara, R.B., Simpson, G.L., Solymos, P., Henry, M., Stevens, H., Wagner, H., 2013. Vegan: community ecology package. R package version 2.0-10. http://CRAN.Rproject.org/package=vegan.
Ortega, P., Lehner, F., Swingedouw, D., Masson-Delmotte, V., Raible, C.C., Casado, M., Yiou, P., 2015. A model-tested north Atlantic oscillation reconstruction for the past millennium. Nature 523, 71-74.
Palacios, D., Andrés,N., Marcos, J., Vázquez-Selem, L., 2012. Maximum glacial advance and deglaciation of the Pinar valley (Sierra de Gredos, Central Spain) and its significance in the Mediterranean context. Geomorphology 177–178, 51–61.
Palacios, D., de Marcos, J., Vázquez-Selem, L., 2011. Last Glacial Maximum and deglaciation of Sierra de Gredos, central Iberian Peninsula. Quat. Int. 233, 16–26.
Parris, A.S., Bierman, P.R., Noren, A.J., Prins, M.A., Lini, A., 2010. Holocene paleostorms identified by particle size signatures in lake sediments from the northeastern United States. J. Paleolimnol. 43, 29–49.
Pedraza, J., 1994. Los modelos genético-evolutivos del Sistema Central Español: Implicaciones morfotectónicas, vol. 13. Cadernos do Laboratorio Xeolóxico de Laxe, pp. 91–118.
Pelto, M.S., 2008. Impact of climate change on north cascade Alpine glaciers, and Alpine runoff. Northwest. Sci. 82, 65–75.
Pérez-Sanz, A., González-Sampériz, P., Moreno, A., Valero-Garcés, B., Gil-Romera, G., Rieradevall, M., Tarrats, P., Lasheras-Álvarez, L., Morellón, M., Belmonte, A., Sancho, C., Sevilla-Callejo, M., Navas, A., 2013. Holocene climate variability, vegetation dynamics and fire regime in the central Pyrenees: the Basa de la Mora sequence (NE Spain). Quat. Sci. Rev. 73, 149–169.
Petzoldt, T., Rinke, K., 2007. Simecol: an object-oriented framework for ecological modeling in R. J. Stat. Soft. 22, 1–31. http://www.jstatsoft.org/v22/i09/.
Pla, S., Catalan, J., 2005. Chrysophyte cysts from lake sediments reveal the submillennial winter/spring climate variability in the northwestern Mediterranean region throughout the Holocene. Clim. Dyn. 24, 263–278.
Pla-Rabes, S., Catalan, J., 2011. Deciphering chrysophyte responses to climate seasonality. J. Paleolimnol. 46, 139–150.
R Core Team, 2015. R: A Language and Environment for Statistical Computing. R Foundation for Statistical Computing, Vienna, Austria. http://www.R-project.org.
Reimer, P.J., Bard, E., Bayliss, A., Beck, J.W., Blackwell, P.G., Ramsey, C.B., Buck, C.E., Cheng, H., Edwards, R.L., Friedrich, M., Grootes, P.M., 2013. INTCAL13 and MARINE13 radiocarbon age calibration curves 0–50,000 years cal BP. Radiocarbon 55, 1869–1887.
Riera, S., Wansard, G., Julià, R., 2004. 2000-year environmental history of a karstic lake in the Mediterranean pre-Pyrenees: the Estanya Lakes (Spain). Catena 55, 293–324. doi:10.1016/S0341-8162(03)00107-3.
Rodrigues, T., Grimalt, J.O., Abrantes, F.G., Flores, J.A., Lebreiro, S.M., 2009. Holocene interdependences of changes in sea surface temperature, productivity, and fluvial inputs in the Iberian continental shelf (Tagus mud patch). Geochem. Geophys. Geosyst. 10. doi: 10.1029/2008GC002367.
Rull, V., Stansell, N.D., Montoya, E., Bezada, M., Abbott, M.B., 2010. Palynological signal of the

Younger Dryas in the tropical Venezuelan Andes. Quat. Sci. Rev. 29, 3045–3056.
Salabarnada, A., 2011. Recent Depositional Evolution of a High Altitude Alpine Lake: Marboré Lake (Ordesa - Monte Perdido National Park, Spanish Pyrenees). MSc Thesis. UIMP University, p. 42.
Sánchez-Cabeza, J.A., Masqué, P., Ani-Ragolta, I., 1998. $^{210}$Pb and $^{210}$Po analysis in sediments and soils by microwave acid digestion. J. Radioanal. Nucl. Chem. 227, 19–22.
Sánchez-López, G., Hernández, A., Pla-Rabes,S., Toro, M., Granados, I., Sigró, J., Trigo, R.M., Rubio-Inglés, M.J., Camarero, L., Valero-Garcés, B., Giralt, S., 2015. The effects of the NAO on the ice phenology of Spanish alpine lakes. Clim. Change 130, 101-113. doi:10.1007/s10584-015-1353-y.
Shabbar, A., Huang, J., Higuchi, K., 2001. The relationship between the wintertime north Atlantic oscillation and blocking episodes in the north Atlantic. Int. J. Climatol. 21, 355–369.
Sigl, M., Winstrup, M., McConnell, J.R., Welten, K.C., Plunkett, G., Ludlow, F., Büntgen, U., Caffee, M., Chellman, N., Dahl-Jensen, D., Fischer, H., Kipfstuhl, S., Kostick, C., Maselli, O.J., Mekhaldi, F., Mulvaney, R., Muscheler, R., Pasteris, D.R., Pilcher, J.R. , Salzer, M., Schüpbach, S., Steffensen, J.P., Vinther, B.M., Woodruff, T.E., 2015. Timing and climate forcing of volcanic eruptions for the past 2,500 years. Nature 523, 543–549. doi: doi.org/10.1038/nature14565.
Sousa, P.M., Barriopedro, D., Trigo, R.M., Ramos, A.M., Nieto, R., Gimeno, L., Turkman, K.F., Liberato, M.L.R., 2015. Impact of euro-Atlantic blocking patterns in Iberia precipitation using a novel high resolution dataset. Clim. Dyn., 1-19. doi:10.1007/s00382-015-2718-7.
Steinhilber, F., Beer, J., Fröhlich, C., 2009. Total solar irradiance during the Holocene. Geophys. Res. Lett. 36. doi:10.1029/2009GL040142.
Stoffel, M., Khodri, M., Corona, C., Guillet, S., Poulain, V., Bekki, S., Guiot, J., Luckman, B.H., Oppenheimer, C., Lebas, N. Beniston, M., Masson-Delmotte, V. 2015. Estimates of volcanic-induced cooling in the Northern Hemisphere over the past 1,500 years. Nature Geoscience. doi:10.1038/NGEO2526.
Stuiver, M., Reimer, P.J., 1993. Extended C-14 data base and revised Calib 3.0 C-14 age calibration program. Radiocarbon 35, 215–230.
Toro, M., Granados, I., Robles, S., Montes, C., 2006. High mountain lakes of Central Range (Iberian Peninsula): regional limnology and environmental changes. Limnetica 25, 217–252.
Trigo, R., Osborn, T., Corte-Real, J., 2002. The north Atlantic oscillation influence on Europe: climate impacts and associated physical mechanisms. Clim. Res. 20, 9–17.
Trigo, R.M., Trigo, I.F., DaCamara, C.C., Osborn, T.J., 2004. Climate impact of the European winter blocking episodes from the NCEP/NCAR reanalyses. Clim. Dyn. 23, 17–28. doi:10.1007/s00382-004-0410-4.
Trigo, R.M., Valente, M.A., Trigo, I.F., Miranda, P.M., Ramos, A.M., Paredes, D., García-Herrera, R., 2008. The impact of north Atlantic wind and cyclone trends on European precipitation and significant wave height in the Atlantic. Ann. N. Y. Acad. Sci. 1146, 212–234. doi:10.1196/annals.1446.014.
Trouet, V., Esper, J., Graham, N.E., Baker, A., Scourse, J.D., Frank, D.C., 2009. Persistent positive north Atlantic oscillation mode dominated the medieval climate anomaly. Science 324, 78–80. doi:10.1126/science.1166349.
Valero-Garcés, B.L., González-Sampériz, P., Navas, A., Machín, J., Mata, P., Delgado-Huertas, A., Bao, R., Moreno, A., Carrión, J.S., Schwalb, A., González-Barrios, A., 2006. Human impact since medieval times and recent ecological restoration in a Mediterranean lake: the Laguna Zoñar, southern Spain. J. Paleolimnol. 35, 441–465.